J. Fluid Mech. (2010), *vol.* 658, *pp.* 463–491. © Cambridge University Press 2010
doi:10.1017/S0022112010001837

Three-dimensional simulations of premixed hydrogen/air flames in microtubes

G. PIZZA[1,2], C. E. FROUZAKIS[1]†, J. MANTZARAS[2],
A. G. TOMBOULIDES[3] AND K. BOULOUCHOS[1]

[1]Aerothermochemistry and Combustion Systems Laboratory, Swiss Federal Institute of Technology, Zurich CH-8092, Switzerland

[2]Combustion Research Laboratory, Paul Scherrer Institute, Villigen CH-5232, Switzerland

[3]Department of Mechanical Engineering, University of Western Macedonia, Kozani 50100, Greece

(Received 6 October 2009; revised 8 April 2010; accepted 12 April 2010)

The dynamics of fuel-lean (equivalence ratio $\phi = 0.5$) premixed hydrogen/air atmospheric pressure flames are investigated in open cylindrical tubes with diameters of $d = 1.0$ and 1.5 mm using three-dimensional numerical simulations with detailed chemistry and transport. In both cases, the inflow velocity is varied over the range where the flames can be stabilized inside the computational domain. Three axisymmetric combustion modes are observed in the narrow tube: steady mild combustion, oscillatory ignition/extinction and steady flames as the inflow velocity is varied in the range $0.5 \leqslant U_{IN} \leqslant 500\,\mathrm{cm\,s^{-1}}$. In the wider tube, richer flame dynamics are observed in the form of steady mild combustion, oscillatory ignition/extinction, steady closed and open axisymmetric flames, steady non-axisymmetric flames and azimuthally spinning flames ($0.5 \leqslant U_{IN} \leqslant 600\,\mathrm{cm\,s^{-1}}$). Coexistence of the spinning and the axisymmetric modes is obtained over relatively wide ranges of U_{IN}. Axisymmetric simulations are also performed in order to better understand the nature of the observed transitions in the wider tube. Fourier analysis during the transitions from the steady axisymmetric to the three-dimensional spinning mode and to the steady non-axisymmetric modes reveals that the $m = 1$ azimuthal mode plays a dominant role in the transitions.

Key words: flames, instability, laminar reacting flows

1. Introduction

Flame propagation in tubes is encountered in many practical applications, including micro- and mesoscale combustion, gas turbines, internal combustion engines and is also relevant for fire hazard and safety. Although several numerical, experimental and theoretical studies have revealed a wealth of phenomena resulting from the complicated interplay of flow, heat and mass transfer, and chemistry, leading to unsteady burning regimes and to complex flame structures, flame propagation in tubes is not fully understood.

Different combustion modes have been reported in experimental and numerical works on premixed flame propagation in ducts: mild or flameless combustion (Maruta *et al.* 2005; Pizza *et al.* 2008*a*), periodic repetitive ignition/extinction (Maruta *et al.*

---

† Email address for correspondence: frouzakis@lav.mavt.ethz.ch

2005; Richecoeur & Kyritsis 2005; Jackson *et al.* 2007; Pizza *et al.* 2008*a*, *b*), steady non-axisymmetric flames in circular ducts (Lewis & von Elbe 1987; Kurdyumov & Fernandez-Tarrazo 2002; Kurdyumov *et al.* 2007; Tsai 2008), or asymmetric steady flames in planar channels (Dogwiler *et al.* 1998; Pizza *et al.* 2008*a*, *b*), tulip flames (Ellis 1928; Dunn-Rankin, Sawyer & Barr 1986; Clanet & Searby 1996; Marra & Continillo 1996; Dunn-Rankin & Sawyer 1998; Bychkov *et al.* 2007), oscillating flames (periodic, quasi-periodic and chaotic) (Maruta *et al.* 2005; Kurdyumov *et al.* 2008; Pizza *et al.* 2008*a*, *b*) and spinning flames (Matkowsky & Olagunju 1982; Kwon, Lee & Chung 1996; Pearlman 1997; Xu & Ju 2007).

Four different combustion modes were observed in the experimental study of Maruta *et al.* (2005) on premixed flame propagation of methane/air and propane/air mixtures in a 2 mm inner diameter straight tube with constant temperature walls, as the inflow velocity was increased from 2 to 100 cm s^{-1}. In addition to two stationary axisymmetric flames (vigorous burning flames at higher velocities and mild or flameless combustion at the lowest velocities), two oscillatory combustion modes were reported at intermediate velocities: a large-amplitude oscillatory extinction and re-ignition mode and a mode characterized by a combination of axial flame pulsations and of ignition/extinction. Steady axisymmetric as well as oscillatory ignition/extinction flames have also been reported in the experiments of Richecoeur & Kyritsis (2005) on methane/oxygen flame propagation in curved ducts with inner diameter ranging from 1 to 4 mm and Reynolds numbers up to 170. The frequency of the ignition/extinction mode increased with decreasing tube diameter.

In other works, non-axisymmetric flame structures have been reported. Kurdyumov *et al.* (2007, 2008), performed experiments on premixed propane/air and methane/air flame propagation in long (1.49 m) and wide (21.4 mm inner diameter) Pyrex tubes for Reynolds numbers up to 150. Besides flame oscillations observed near the flashback limit (Kurdyumov *et al.* 2008), a steady non-axisymmetric flame was observed for high flow rates (Kurdyumov *et al.* 2007), similar to the 'tilted' flame described by Lewis & von Elbe (1987). In the experiments of Dogwiler *et al.* (1998), asymmetric flames, anchored on either the upper or the lower wall, were recorded in fuel-lean CH_4/air mixtures combustion in a rectangular channel with a height of 7 mm. The sensitivity of the asymmetric flame to external perturbations resulted in transitions between the two flame structures at seemingly random time intervals.

In certain configurations, spinning flames have been observed. Kwon *et al.* (1996) recorded spinning premixed methane/air and propane/air flames in a sudden expansion tube for equivalence ratios close to the blow-off limit. Preferential diffusion and heat loss to the walls were proposed as possible mechanisms for the onset of this mode. Pearlman (1997) studied experimentally premixed flames propagating in a quiescent high-Lewis-number butane/oxygen/helium mixture in tubes of inner diameter ranging from 5.1 to 28.5 cm. One end of the tube was open and the mixture was ignited at the opposite, closed end. When the butane concentration was reduced towards the lean flammability limit, the steady propagating flame developed instabilities in the form of travelling and rotating spiral waves. In particular, the spiral waves rotated clockwise or counter-clockwise at frequencies up to 100 Hz. The author attributed this instability to the diffusive thermal imbalance of the fuel in the mixture (Lewis number $Le > 4$). More recently, Xu & Ju (2007) reported spinning flames in their laminar flame propagation experiments, which were carried out in a mesoscale divergent quartz tube (internal diameter $4 \leqslant d \leqslant 10$ cm) with methane/air and propane/air mixtures at lean and rich conditions. When the inflow velocity was reduced below a critical value, the spinning flame turned into a stationary symmetric flame. Flame/wall coupling and thermal diffusion in the gas and solid phases were suggested as the processes governing the flame dynamics. Spinning combustion waves have also been observed in different configurations like radial microchannels (Zamashchikov 2003), porous plug burner (Robbins *et al.* 2004) and in combustion of solid cylindrical samples (Maksimov *et al.* 1979; Zhang & Munir 1992).

Another feature encountered, when a flame propagates in a tube starting from a localized ignition source, is the tulip flame phenomenon, which is characterized by the inversion of the flame curvature from convex to concave towards the unburnt mixture. The tulip flame was first reported many years ago by Ellis (1928); more detailed information on the flow and pressure field in the tube and flame imaging were provided recently in the experiments of Clanet & Searby (1996) and Dunn-Rankin & Sawyer (1998).

Flame propagation in tubes has also been extensively studied by means of numerical simulations. However, due to high computational cost, simplified models were usually adopted: the thermodiffusive or constant-density model, single-step chemistry, symmetry conditions and/or steady formulation. The flame modes observed experimentally by Maruta *et al.* (2005) and Richecoeur & Kyritsis (2005) were numerically reproduced by Maruta *et al.* (2005), Minaev, Maruta & Fursenko (2007) and Jackson *et al.* (2007), using an *ad-hoc* simplified one-dimensional thermodiffusive model, and by Kurdyumov *et al.* (2009) using a two-dimensional thermodiffusive model. Kurdyumov *et al.* (2008) used a constant-density model taking into account heat conduction in the walls to obtain similar behaviour as the experimentally observed flame oscillations near flashback. The spiral waves reported in the experiments of Pearlman (1997) were numerically studied by Scott, Wang & Showalter (1997) using a simplified two-dimensional reaction–diffusion model with heat losses and a constant source of fuel in order to sustain the reaction. They showed that, unlike the observations of Pearlman (1997), spiral flames also arise for $Le < 1$.

The same simplified two-dimensional model was used by Panfilov, Bayliss & Matkowsky (2003) with parameters more representative of combustion, giving both periodic and meandering spiral flames. There have also been a number of numerical simulations aiming at reproducing the tulip flame and clarifying the underlying physical mechanisms. Marra & Continillo (1996) used a low-Mach-number formulation with cylindrical symmetry and single-step chemistry, to study the transient laminar flame propagation in a closed cylinder, and proposed the flame/wall interaction as the driving mechanism leading to the tulip flame. Using an evolution equation in the limit of weak thermal expansion, Matalon & Metzener (1997) suggested the vorticity generation due to the flame front as the mechanism leading to the tulip flame. Other explanations based on the available experimental evidence and numerical results have also been proposed (Dunn-Rankin *et al.* 1986; Gonzalez, Borghi & Saouab 1992, etc.); however, the actual conditions for the appearance of the tulip flame are not yet completely understood (Bychkov *et al.* 2007).

In our recent simulations of combustion in micro- (Pizza *et al.* 2008*b*) and mesoscale (Pizza *et al.* 2008*a*) two-dimensional channels with detailed chemistry and transport, complex flame dynamics was found in ducts having constant temperature and chemically inert (non-catalytic) walls. Depending on the inflow velocity and the channel height, up to six combustion modes were observed, including not only those observed experimentally in Maruta *et al.* (2005), Richecoeur & Kyritsis (2005) and Dogwiler *et al.* (1998), but also additional oscillating flame modes with cellular structure and chaotic behaviour; some of these modes were found to coexist over a range of inflow velocities. In another related work, Pizza *et al.* (2009) have shown that the unsteady and asymmetric modes of the inert channels can be effectively suppressed by controlling the catalytic reactivity on the channel walls.

Only few numerical works take into account three-dimensional computational domains without invoking axisymmetry. Kurdyumov & Fernandez-Tarrazo (2002) simulated propagating flames in open ducts of circular cross-section with adiabatic and isothermal walls using a transient constant-density model with non-unity Lewis number. For $Le < 1$, stationary complex three-dimensional flame structures were observed when the ratio between the tube radius and the flame thickness exceeded a critical value. Recently, Tsai (2008) investigated the steady propagation of flames in isothermal axisymmetric and three-dimensional tubes of different diameter by solving the steady conservation equations for a $Le = 1$ methane/air mixture. It was found that for tubes with diameters larger than a critical value, only non-axisymmetric flame structures are possible, supporting the findings of Kurdyumov & Fernandez-Tarrazo (2002).

Some of the experimentally and numerically observed modes have also been studied theoretically. Spinning combustion waves were predicted by Matkowsky & Olagunju (1982), who analyzed the stability of premixed flame fronts propagating in cylindrical tubes using a thermodiffusive model. It was reported that when the Lewis number exceeds a critical value larger than unity, a uniformly propagating plane flame becomes unstable and, depending on the tube radius, various types of solutions arise. When the radius is smaller than a critical value, the solution is a planar pulsating flame, whereas at larger radii, radial and tangential modes appear, which can be either spinning or standing waves. Petchenko & Bychkov (2004) studied the stability of a flame in a cylindrical tube having adiabatic slip walls with respect to non-axisymmetric perturbations, by performing linear stability analysis using a time-dependent nonlinear equation for the flame surface. For a tube radius above a critical value that is proportional to the cutoff wavelength of the Darrieus–Landau instability, infinitesimal non-axisymmetric perturbations on the flame front grow exponentially, indicating that only three-dimensional non-axisymmetric flame structures can be expected. Besides, heat losses to the tube walls increase the range of stability of axisymmetric flames. In a way, these results are in contrast with the earlier work of Metzener & Matalon (2001); therein, by means of numerical simulation based on an evolution equation similar to Petchenko & Bychkov (2004) (and thus in the limit of weak thermal expansion), it was shown that for sufficiently large tube radii and under certain initial conditions, the flame shape settled down to an axisymmetric configuration.

A comprehensive three-dimensional numerical study on unsteady flame propagation in cylindrical tubes is still missing. In this work, transient numerical simulations with detailed chemistry and transport and taking into account the entire three-dimensional domain are performed to study unsteady flame propagation in cylindrical tubes. A fuel-lean, $\phi = 0.5$, H_2/air mixture is fed into prescribed wall-temperature tubes having inner diameters of 1.0 and 1.5 mm and inflow velocities covering the full range over which the flames can be stabilized within the tube. In the narrow tube, three axisymmetric flame modes are observed: mild combustion, ignition/extinction, and symmetric steady flames. In addition to these modes, also spinning and steady non-axisymmetric flames are obtained in the wider tube. Fourier mode analysis is used to characterize the transitions.

This article is organized as follows: § 2 describes the three-dimensional transient computational model. In §§ 3 and 4, the flame dynamics in the $d = 1$ and $d = 1.5$ mm diameter tubes are discussed in detail. Results of axisymmetric simulations are presented in § 5, while in § 6 Fourier analysis is used to analyse of the transitions between the modes. Finally, § 7 summarizes the key results of this investigation.

2. Formulation

2.1. *Governing equations*

The governing equations considered in this study are the Navier–Stokes equations together with the energy and chemical species conservation equations at the low-Mach-number limit for open systems together with the equation of state (ideal gas law).

At the low-Mach-number limit ($Ma \rightarrow 0$), the pressure appears at leading order in terms of Ma^2 in the energy and state equations ('thermodynamic pressure' p_0), and at first order in the momentum equation ('hydrodynamic pressure' p_1) (Chu & Kovasznay 1958; Rehm & Baum 1978; Majda 1984). Acoustic waves are neglected – thereby facilitating numerical integration – while compressibility effects due to heat release and composition changes are fully retained. This formulation is well suited for a large range of combustion applications, which involve low-speed flows.

Continuity

$$\frac{\partial \rho}{\partial t} + \nabla \cdot (\rho \boldsymbol{u}) = 0. \tag{2.1}$$

Momentum

$$\rho \left(\frac{\partial \boldsymbol{u}}{\partial t} + \boldsymbol{u} \cdot \nabla \boldsymbol{u} \right) = -\nabla p_1 + \nabla \cdot (\mu \boldsymbol{S}). \tag{2.2}$$

Energy

$$\rho c_p \left(\frac{\partial T}{\partial t} + \boldsymbol{u} \cdot \nabla T \right) = \nabla \cdot (\lambda \nabla T) - \sum_{i=1}^{N_g} h_i \dot{\omega}_i - \rho \left(\sum_{i=1}^{N_g} c_{p,i} Y_i \boldsymbol{V}_i \right) \cdot \nabla T. \tag{2.3}$$

Species

$$\rho \left(\frac{\partial Y_i}{\partial t} + \boldsymbol{u} \cdot \nabla Y_i \right) = -\nabla \cdot (\rho Y_i \boldsymbol{V}_i) + \dot{\omega}_i \qquad i = 1, \ldots, N_g. \tag{2.4}$$

Ideal gas law

$$p_0 = \rho \frac{R}{\overline{W}} T. \tag{2.5}$$

In the low-Mach-number formulation, (2.1) is replaced by (2.6) below, which is obtained by combining the continuity (2.1), energy (2.3), species (2.4), and state (2.5) equations:

$$\begin{aligned} \nabla \cdot \boldsymbol{u} = -\frac{1}{\rho} \left(\frac{\partial \rho}{\partial t} + \boldsymbol{u} \cdot \nabla \rho \right) &= \frac{1}{\rho} \sum_{i=1}^{N_g} \frac{\overline{W}}{W_i} (-\nabla \cdot \rho Y_i \boldsymbol{V}_i + \dot{\omega}_i) \\ &+ \frac{1}{\rho c_p T} \left[\nabla \cdot (\lambda \nabla T) - \sum_{i=1}^{N_g} h_i \dot{\omega}_i - \rho \left(\sum_{i=1}^{N_g} c_{p,i} Y_i \boldsymbol{V}_i \right) \cdot \nabla T \right]. \end{aligned} \tag{2.6}$$

In (2.1)–(2.6), ρ, $\boldsymbol{u}$, μ, T and λ are the density, velocity vector, dynamic viscosity, temperature and mixture thermal conductivity, respectively; Y_i, $\boldsymbol{V}_i$, W_i, $c_{p,i}$, h_i and $\dot{\omega}_i$ are the mass fraction, diffusion velocity vector, molecular weight, heat capacity, enthalpy and the chemical source term of the ith species, respectively, $\overline{W}$ is the mean molecular weight of the mixture and R the ideal gas constant. Gravity and radiation effects were neglected in the simulations. The stress tensor and the mixture heat capacity are

$$\boldsymbol{S} = \nabla \boldsymbol{u} + (\nabla \boldsymbol{u})^T - \tfrac{2}{3}(\nabla \cdot \boldsymbol{u})\boldsymbol{I} \tag{2.7}$$

$$c_p = \sum_{i=1}^{N_g} c_{p,i} Y_i, \tag{2.8}$$

respectively, and $\boldsymbol{I}$ is the identity matrix. In total, there are N_g chemical species participating in the reaction mechanism. For a generic reversible reaction

$$\sum_{i=1}^{N_g} \nu'_{ij} M_i \rightleftharpoons \sum_{i=1}^{N_g} \nu''_{ij} M_i, \qquad j = 1, \ldots, N_R, \tag{2.9}$$

in a detailed mechanism of N_R elementary reactions among species M_i, $i = 1, \ldots, N_g$, the rate of reaction j is, according to the law of mass action, given in terms of the products of the molar concentrations of the species $[X_i] = \rho Y_i / W_i$ by

$$r_j = k_j^f \prod_{i=1}^{N_g} [X_i]^{\nu'_{ij}} - k_j^r \prod_{i=1}^{N_g} [X_i]^{\nu''_{ij}} \tag{2.10}$$

where ν'_{ij}, ν''_{ij} are the stoichiometric coefficients of species i in the forward and reverse direction, respectively. The forward rate constant k_j^f of reaction j follows an Arrhenius-type temperature dependence

$$k_j^f = A_j \, T^{\beta_j} \exp\left(\frac{-E_j}{R\,T}\right), \tag{2.11}$$

with the pre-exponential factor A_j, the temperature exponent β_j and the activation energy E_j specified as part of the detailed reaction scheme; the forward and reverse reaction rate constants are related through the equilibrium constant $K_{c,j}(T) = k_j^f / k_j^r$. The mass production/consumption rate of species i is the sum of the rates of progress r_j of all reactions $j = 1, \ldots, N_R$ involving the ith species:

$$\dot{\omega}_i = W_i \sum_{j=1}^{N_R} \nu_{ij} r_j, \tag{2.12}$$

with $\nu_{ij} = \nu''_{ij} - \nu'_{ij}$.

The species diffusion velocities $\boldsymbol{V}_i$ are given by

$$\boldsymbol{V}_i = \boldsymbol{V}_i^* + \boldsymbol{V}_c, \tag{2.13}$$

where $\boldsymbol{V}_i^*$ is obtained from the kinetic theory of gases (Hirschfelder, Curtiss & Bird 1954) considering mixture-averaged diffusion and neglecting pressure and thermal diffusion,

$$\boldsymbol{V}_i^* = -(D_{mi}/X_i)\nabla X_i, \tag{2.14}$$

D_{mi} and $X_i = Y_i \overline{W} / W_i$ are the ith species mixture-average diffusivity and molar fraction, respectively. The second term in (2.13) is the correction velocity introduced

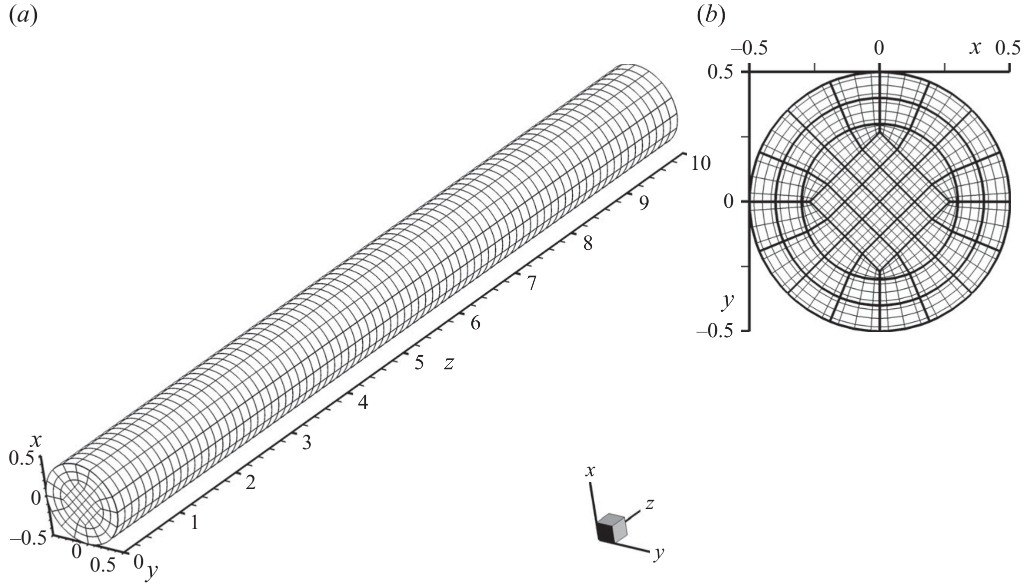

FIGURE 1. The computational grid: 5120 elements with fourth-order polynomials in each spatial direction. The spectral element skeleton is shown in (*a*); in (*b*) the thick lines mark the elemental boundaries, and the intersections between all the lines (thin and thick) represent the Gauss–Lobatto–Legendre quadrature points ($N_x = N_y = N_z = N_p + 1$; here, $N_p = 4$).

to guarantee numerically total mass conservation (Coffee & Heimerl 1981)

$$\boldsymbol{V}_c = -\sum_{i=1}^{N_g} Y_i \boldsymbol{V}_i^*. \tag{2.15}$$

2.2. *Solution method*

The governing equations (2.1)–(2.6) are solved using the spectral element method for spatial discretization, a high-order weighted residual method that combines the tensor product efficiency of global spectral methods with the geometric flexibility of finite elements. The computational domain is split into deformed quadrilateral (in two-dimensional) or hexahedral (in three-dimensional) conforming elements (see figure 1). Locally, the mesh is structured and the solution, data and geometry are expressed as sums of tensor product N_p-order Lagrange polynomials, based on the Gauss–Lobatto–Legendre quadrature points (Patera 1984; Deville, Fischer & Mund 2002).

Time integration of the discretized equations is performed using a high-order splitting scheme for low-Mach-number reactive flows. The continuity and momentum equations are integrated with a semi-implicit scheme (Tomboulides, Lee & Orszag 1997), whereas the species and energy equations are integrated implicitly using the CVODE solver (Cohen & Hindmarsh 1996). Details on the mathematical formulation, the numerical method, as well as validation of the approach with asymptotic analysis and numerical benchmark tests can be found in Tomboulides & Orszag (1998).

Within the fixed non-dimensional time step Δt used for the hydrodynamics (time is non-dimensionalized with respect to the inflow velocity U_{IN} and the tube diameter d, typically $\Delta t = 5 \times 10^{-5}$), the integration time step for thermochemistry is automatically adapted by CVODE in order to satisfy the chosen relative (10^{-7}) and absolute (10^{-8}) tolerances.

The simulations were performed using a highly scalable parallel code based on the NEK5000 code (Fischer, Lottes & Kerkemeier 2008) on Linux clusters. The computational time strongly depends on the domain size and the combustion mode: for example, for the long transients of the non-stationary solutions in the 1.5 mm diameter three-dimensional tube, up to 500 h on thirty-two 2.6 GHz CPUs are required.

2.3. *Computational set-up*

A fuel-lean atmospheric pressure H_2/air premixed mixture with equivalence ratio $\phi = 0.5$ is fed at the inlet of a cylindrical tube with length L and aspect ratio $L/d = 10$, leading to channel lengths of 10 and 15 mm for the examined tube diameters. Such short lengths are of prime interest for microreactors used in portable power generation (see e.g. Maruta *et al.* 2002; Norton & Vlachos 2003; Karagiannidis *et al.* 2007). Uniform inlet velocity U_{IN}, constant inlet temperature $T_{IN} = 300\,\mathrm{K}$ and flux conditions for the incoming species mass fractions

$$\rho Y_i V_{i,x} = \rho U_{IN}(Y_{i,IN} - Y_i) \tag{2.16}$$

are specified at the inflow, where $Y_{i,IN}$ is the mass fraction of species i in the incoming mixture. At the gas–wall interface, no-slip for both velocity components and zero-flux for all species is applied.

The wall temperature is prescribed: over the initial 1/20 domain length, it ramps smoothly via a hyperbolic tangent function from the temperature of the incoming mixture T_{IN} to the final value $T_W = 960\,\mathrm{K}$. The final wall temperature was selected so as to be tolerable by materials used for microreactors. A wide variety of steels (class 400) commonly used for reactor construction have maximum operational temperatures around 960 K. Higher wall temperatures (up to 1400 K) can be tolerated by ceramic materials. However, at such temperatures the high reactivity of hydrogen leads to flames anchored close to the channel entry and unrealistically high velocities ($U_{IN} > 150\,\mathrm{m\,s^{-1}}$) are required to shift the anchoring point downstream. The smooth ramping of temperature has physical attributes. In a practical combustor, the heat losses at the entry section (radiation from the reactor front to the cold surroundings and convective cooling due to the impingement of the cold incoming flow on the vertical face of the reactor walls) results in a temperature profile with an initial ramp. Heat conduction in the solid and the large heat capacity of the solid walls result in a fairly constant and quasi-steady (with respect to the fast flame dynamics) temperature profile along the remaining length of the wall. Similar wall-temperature conditions were realized in other experimental (Maruta *et al.* 2005) and numerical (Raja *et al.* 2000; Mantzaras & Appel 2002; Pizza *et al.* 2008*a*,*b*) studies. At the outlet, zero-Neumann boundary conditions are imposed for all variables.

The gas-phase chemistry is described by the detailed reaction mechanism of Kim, Yetter & Dryer (1994) with 9 chemical species (H_2, O_2, H_2O, H, O, OH, HO_2, H_2O_2, N_2) and 21 reversible elementary reactions; the reaction rates are evaluated using the CHEMKIN package (Kee, Rupley & Miller 1989). A mixture-average transport model is adopted for the species diffusion velocities (defined in (2.14)), using the CHEMKIN transport database (Kee *et al.* 1986).

The structure of the one-dimensional freely propagating adiabatic lean premixed laminar H_2/air flame for the equivalence ratio and inflow temperature considered in this study is computed using the PREMIX code of CHEMKIN (Kee *et al.* 1985). The laminar flame speed is $S_L = 58\,\mathrm{cm\,s^{-1}}$, while the thermal flame thickness δ_f is evaluated as

$$\delta_f = \frac{T_f - T_{IN}}{max \left| \dfrac{\partial T}{\partial x} \right|} = 0.4\,\mathrm{mm}. \tag{2.17}$$

Here, $T_f = 1630\,\mathrm{K}$ is the maximum flame temperature, and $max\ |\partial T/\partial x|$ the maximum temperature gradient along the flame coordinate.

2.4. *Computational domain*

The three-dimensional cylindrical domain is discretized with a total of 5120 spectral elements (64 in the radial and azimuthal plane and 80 equally spaced in the streamwise direction), as shown in figure 1(*a*). On a plane perpendicular to the flow direction shown in figure 1(*b*), the thick lines represent elemental boundaries, while the intersections of all lines (thin and thick) are the interpolation points for $N_p = 4$.

The presence of many chemical species with reaction layers of different thickness (some, like the HO_2 radical, with thickness smaller than δ_f) renders an a priori estimation of resolution requirements difficult. The minimum resolution must at least properly resolve the thermal flame thickness δ_f, whereas the adequacy of the grid was assessed a posteriori by refinement tests. Thus, a grid with the given number of spectral elements was constructed, and then simulations were performed at increasing polynomial orders N_p in order to obtain a grid-independent solution.

For the $d = 1.5\,\mathrm{mm}$ tube, the fourth-order Legendre–Lagrange interpolating polynomials in each direction result in an average spatial resolution of $\Delta z = 0.047\,\mathrm{mm}$, $\Delta r = 0.037\,\mathrm{mm}$ and $r_{out}\Delta\theta = 0.074\,\mathrm{mm}$ (the latter evaluated at the tube radius r_{out}, with $\Delta\theta$ denoting the angular discretization of the outer cross-sectional area), resulting to approximately $\delta_f/\Delta z = 8$, $\delta_f/\Delta r = 11$, $\delta_f/(r_{out}\Delta\theta) = 5$ grid points within the thermal flame thickness δ_f.

The grid independence of the solution was verified by increasing the polynomial order to 6 without observing any appreciable variation in the solution. The fact that the thermochemical part (species and energy equations) is solved fully implicitly has the additional advantage of avoiding the restrictive Courant number limitations of the small time scales associated with the highly reactive radicals. Since the same computational grid is also used for the $d = 1.0\,\mathrm{mm}$ tube, no resolution analysis was required for the narrow tube. The total number of uniquely counted computational points with $N_p = 4$ is 339 297. At each grid point fourteen variables (three velocity components, pressure, temperature and nine chemical species) must be solved for, resulting in a total of about 4.75 million unknowns.

2.5. *Conditions analysed*

Two tube diameters, $d = 1.0$ and $1.5\,\mathrm{mm}$, are investigated, and the inflow velocity U_{IN} is varied in the range that allows the flame to be stabilized within the computational domain ($0.5 \leqslant U_{IN} \leqslant 500\,\mathrm{cm\,s^{-1}}$ and $0.5 \leqslant U_{IN} \leqslant 600\,\mathrm{cm\,s^{-1}}$ for $d = 1.0$ and $1.5\,\mathrm{mm}$, respectively). For the considered ranges of U_{IN}, the flow is laminar with inlet Reynolds numbers Re_{IN} (based on the tube diameter d, the inflow velocity U_{IN} and the inlet mixture kinematic viscosity $\nu = 0.189\,\mathrm{cm^2\,s^{-1}}$) in the range $0.27 \leqslant Re_{IN} \leqslant 265$ and $0.4 \leqslant Re_{IN} \leqslant 477$ for $d = 1.0$ and $1.5\,\mathrm{mm}$, respectively.

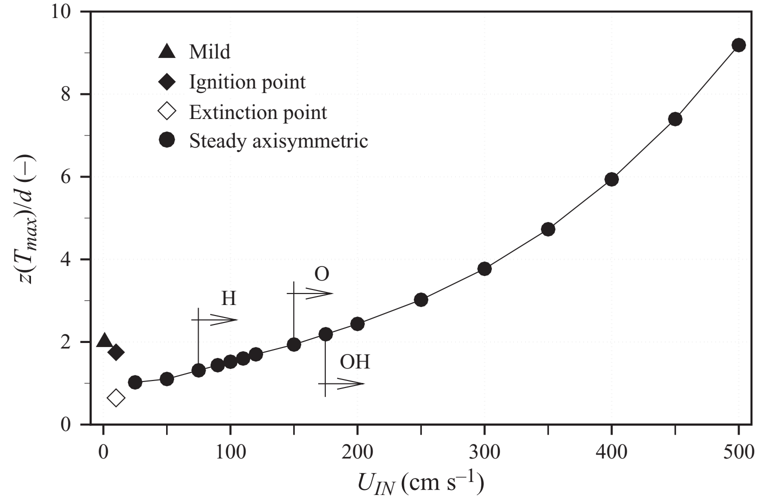

FIGURE 2. Flame stability diagram for the $d = 1.0$ mm tube showing the normalized streamwise distance of the maximum temperature location versus the inflow velocity. The vertical lines mark the value of U_{IN} where the maximum of the mass fraction distribution of the corresponding species is first observed to move away from the tube axis ($U_{IN} = 75$ cm s^{-1} for H, 150 cm s^{-1} for O and 175 cm s^{-1} for OH).

3. Flame dynamics in the 1.0 mm diameter tube

Three axisymmetric flame structures are observed in the narrow tube as the inlet velocity U_{IN} is varied. The observed combustion modes are summarized in figure 2 in terms of $z(T_{max})/d$, the normalized streamwise distance of the maximum temperature location from the inlet, versus the inflow velocity U_{IN} : mild combustion at the lowest U_{IN} (closed triangles), periodic ignition/extinction at intermediate U_{IN} (filled and open diamonds marking the ignition and extinction locations, respectively), and, finally, steady axisymmetric flames at larger U_{IN} (filled circles). The latter mode persists until the flame is blown out of the computational domain.

3.1. *Mild combustion*

Mild combustion, characterized by a very low temperature rise, and incomplete but substantial fuel conversion, is observed for the lowest inflow velocities considered in this study, $0.5 \leqslant U_{IN} \leqslant 1.0$ cm s^{-1}. As can be inferred from the profiles of temperature and species mass fractions along the tube axis for $U_{IN} = 1.0$ cm s^{-1} (figure 3*a*), the reaction is frozen at a state preceding thermal runaway. Due to the low temperature kinetics of hydrogen, the inflowing fuel is converted to hydroperoxy radical (HO_2), hydroxyperoxide (H_2O_2) and water only, while the radicals H, O, OH, associated with the high temperature kinetics reached after thermal runaway are practically absent. A significant amount of fuel is converted (75 % at $U_{IN} = 1.0$ cm s^{-1}), while the rest escapes at the outflow together with H_2O_2 and HO_2. The non-zero axial species gradients at $z = 0$ mm in figure 3(*a*) are due to the flux boundary conditions applied at the inlet. The maximum temperature increase is a mere 1.5 K (at $z = 2.2$ mm) and 2.5 K (at $z = 2.0$ mm) above the 960 K wall temperature for $U_{IN} = 0.5$ and 1.0 cm s^{-1}, respectively. This mode is axisymmetric in shape, and is qualitatively similar to the mild combustion mode observed in both the two-dimensional plane channel simulations of Pizza *et al.* (2008*a*) and the tubular duct experiments of Maruta *et al.* (2005).

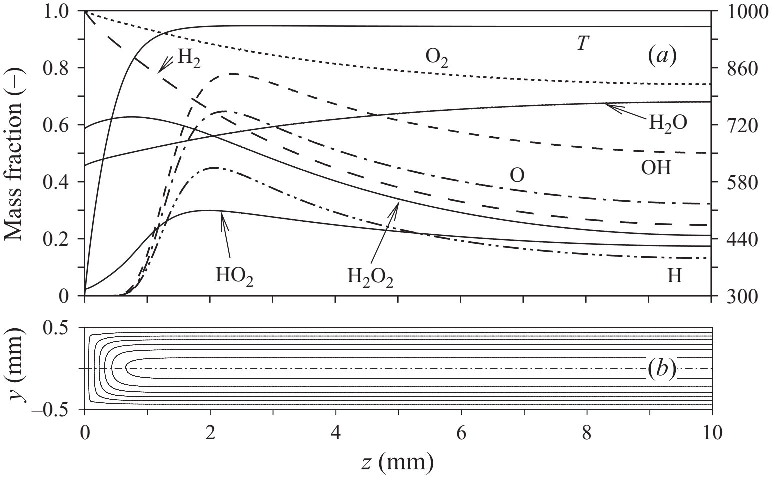

FIGURE 3. Mild combustion at $U_{IN} = 1\,\mathrm{cm\,s^{-1}}$ in the $d = 1.0\,\mathrm{mm}$ tube: (a) scaled species mass fractions ($2.07 \times 10^2 Y_{H_2}$, $5.4 Y_{O_2}$, $7.69 Y_{H_2O}$, $3.33 \times 10^6 Y_H$, $7.14 \times 10^5 Y_{OH}$, $6.25 \times 10^5 Y_O$, $3.33 \times 10^3 Y_{HO_2}$, $2.5 \times 10^3 Y_{H_2O_2}$) and temperature along the tube axis, (b) six iso-lines of the axial velocity component in the $x = 0$ plane, uniformly distributed over the range 1.5–6 $\mathrm{cm\,s^{-1}}$. In (b) the iso-lines above the symmetry axis refer to the reactive case, those below the axis to the non-reactive case.

As expected, the very low heat release of this combustion mode leaves the velocity field practically unaffected. Figure 3(b) shows iso-lines of the axial velocity component w in the y–z plane at $U_{IN} = 1.0\,\mathrm{cm\,s^{-1}}$ for two cases: the iso-lines above the symmetry axis refer to the reactive case, whereas the ones below the axis were obtained with the same hydrogen/air mixture at the inflow as in the reactive case but with the chemical reactions turned off. The maximum difference in velocity between the two cases is 0.16 %.

3.2. *Ignition/extinction*

At slightly higher inflow velocities, the increased convective flux together with the resulting higher total heat release, effectively counteract the heat losses to the walls and establish the conditions for auto-ignition of the mixture. For these inflow velocities, the channel behaves in terms of heat transfer like a plug-flow reactor, and high temperatures leading to auto-ignition are reached along the centreline. Yet, the incoming flux is too low to sustain a steady flame. After ignition two distinct flame fronts form, one propagating upstream and the other downstream until they both extinguish, as will be explained below. After extinction, the channel is filled again with fresh mixture, the radical pool builds up, and a new ignition followed by flame propagation is observed. This combustion mode, characterized by a periodic repetition of flame ignition and extinction, has been reported in experiments (Maruta *et al.* 2005; Richecoeur & Kyritsis 2005) and simulations (Maruta *et al.* 2005; Jackson *et al.* 2007; Pizza *et al.* 2008*a*,*b*), and will be referred to as the ignition/extinction mode.

Details of the ignition/extinction mode at $U_{IN} = 10\,\mathrm{cm\,s^{-1}}$ are shown in figure 4. The temporal evolution of the heat release rate (HRR) integrated over the entire tube and normalized with respect to the density and the enthalpy of the fresh mixture (figure 4a) reveals long periods of relative inactivity, associated with the flow of fresh mixture into the tube and the buildup of the radical pool, followed by sudden bursts, associated with radical and eventually thermal runway and subsequent fast flame

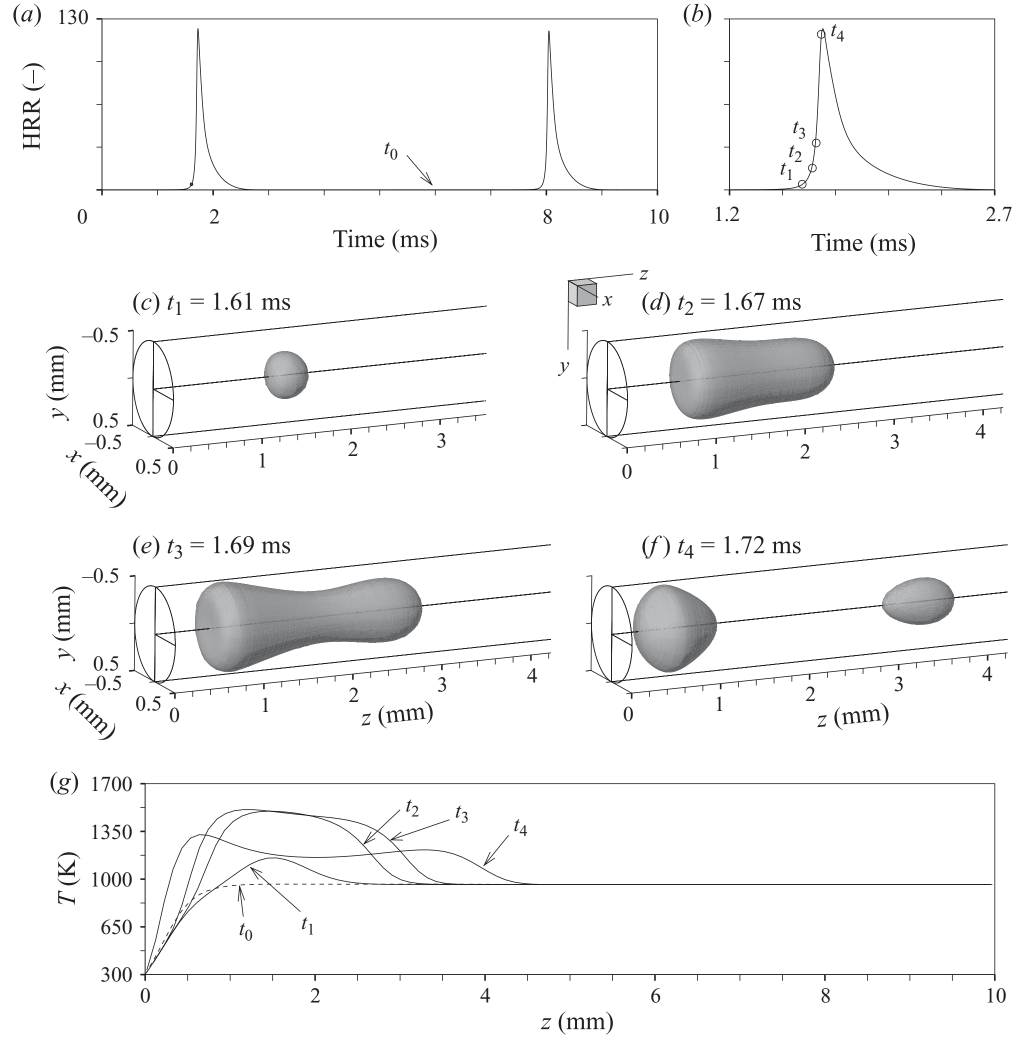

FIGURE 4. Ignition/extinction mode at $U_{IN} = 10\,\mathrm{cm\,s^{-1}}$ in the $d = 1.0$ mm tube: (*a*) temporal variation of the integral heat release rate (HRR); (*b*) expanded detail of (*a*); (*c–f*) three-dimensional iso-surfaces of Y_{OH} ($Y_{\mathrm{OH}} = 9.3 \times 10^{-4}$, 2.2×10^{-3}, 1.6×10^{-3}, and 5×10^{-4} in (*c–f*), respectively) at the four times t_1–t_4 marked in (*b*); (*g*) temperature profiles along the tube axis at time $t_0 = 6$ ms, marked in (*a*), and at times t_1–t_4, marked in (*b*).

propagation. The transient flame structure can be deduced from the Y_{OH} iso-surfaces (figure 4*c–f*) at the four time instants marked in figure 4(*b*). During the periodic process, the maximum temperature varies from the wall temperature (HRR almost zero) to the value of 1520 K, figure 4(*g*). The cold mixture entering the channel is heated up by the hot walls, auto-ignites at $z \approx 1.5$ mm (figure 4*c*), and then forms flame fronts that propagate upstream and downstream (figure 4*d*,*e*), consuming the fuel along their way. The initial ignition kernel is almost spherical and becomes elliptical when part of the flame front reaches the tube walls. The upstream propagating front extinguishes when it reaches the cold inlet section, while the downstream propagating one extinguishes when the local H_2 concentration drops below the lean flammability limit (figure 4*f*). The upstream and the downstream propagating flames extinguish at $z \approx 0.6$ and $z \approx 3.5$ mm, respectively.

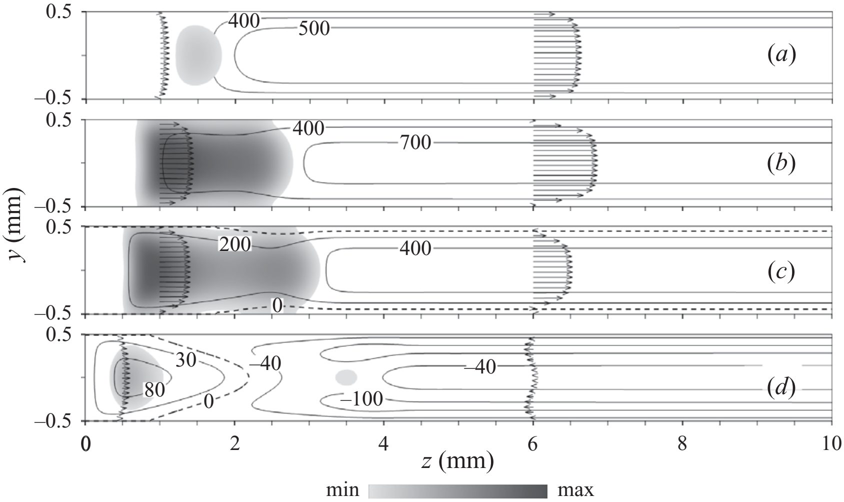

FIGURE 5. Ignition/extinction mode at $U_{IN} = 10\,\mathrm{cm\,s^{-1}}$ in the $d = 1.0$ mm tube: (*a*–*d*) iso-lines of the axial velocity component w and iso-contours of Y_{OH} in the $x = 0$ plane at the four time instants t_1–t_4 marked in figure 4(*b*), respectively. The dashed lines in (*c*) and (*d*) represent the iso-lines with zero axial velocity w, which ranges between $0 \leqslant w \leqslant 535\,\mathrm{cm\,s^{-1}}$, $0 \leqslant w \leqslant 721\,\mathrm{cm\,s^{-1}}$, $-51 \leqslant w \leqslant 441\,\mathrm{cm\,s^{-1}}$ and $-121 \leqslant w \leqslant 95\,\mathrm{cm\,s^{-1}}$, in (*a*–*d*), respectively. The complex flow field is shown by velocity vectors at selected axial locations. The range of the OH mass fraction isocontours is $7 \times 10^{-4} \leqslant Y_{\mathrm{OH}} \leqslant 4 \times 10^{-3}$.

The whole process repeats itself periodically with a constant frequency of 158 Hz, while the flame always maintains an axisymmetric structure. It is interesting to observe that during propagation, the upstream flame front changes curvature from initially convex towards the unburnt mixture (figure 4*d*) to concave (figure 4*e*) and finally convex again when the front approaches the temperature ramping section at the inflow (figure 4*f*); similar behaviour is observed in the tulip flame phenomenon (Ellis 1928; Clanet & Searby 1996; Marra & Continillo 1996; Matalon & Metzener 1997). The downstream propagating front always maintains its initial convex shape towards the fresh mixture. The velocity of the upstream propagation, obtained from the time derivative of the flame location z_f (z_f being the axial coordinate of the point on the axis where Y_{OH} is maximum), reaches its maximal value of around $11\,\mathrm{m\,s^{-1}}$ shortly after ignition. Such a high propagation speed, much higher than the laminar flame velocity $S_L = 58\,\mathrm{cm\,s^{-1}}$, can be explained considering that, due to the preheat from the hot walls, the temperature and the composition of the mixture in which the flame propagates are no longer those of the inflowing mixture (see the temperature profiles in figure 4*g*). The propagation speed of this diffusionally imbalanced mixture is further enhanced by the flame curvature.

Details of the flow fields are provided in figure 5, where the two-dimensional iso-lines of the axial velocity component w on the plane $x = 0$ are presented at the four time instants marked in figure 4(*b*). The dashed lines in figure 5(*c*–*d*) represent the zero axial velocity iso-line. It is evident that a recirculation zone is formed at time t_3 close to the tube walls (figure 5*c*), whereas at time t_4 the flow reverses in part of the domain following the upstream propagating flame front (figure 5*d*).

It is worth noting here that the observed ignition behaviour, namely that the flame is ignited at the tube centre close to the cold inflow, results from the wall heat transfer at the low inflow velocities supporting the ignition/extinction mode. At significantly

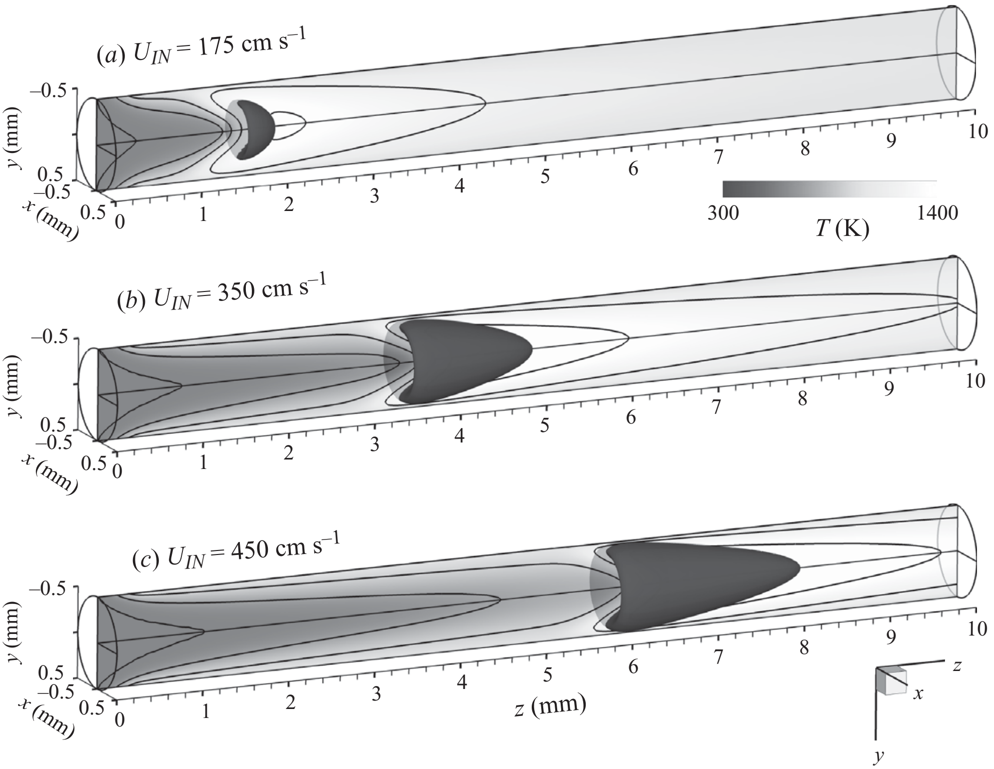

FIGURE 6. Steady axisymmetric flames in the $d = 1.0$ mm tube for inflow velocities (*a*) $U_{IN} = 175\,\mathrm{cm\,s^{-1}}$, (*b*) $350\,\mathrm{cm\,s^{-1}}$ and (*c*) $450\,\mathrm{cm\,s^{-1}}$: three-dimensional iso-surfaces of $Y_{\mathrm{OH}} = 2.4 \times 10^{-3}$ (cone-shaped structure), and iso-contours of temperature on the $x = 0$ plane with five iso-lines (uniformly distributed over the range 301–1400 K).

higher U_{IN}, the thermal boundary layers cannot merge and ignition is observed at the rear end of the reactor close to the hot walls.

3.3. *Steady axisymmetric flame*

When the inflow velocity is increased from 10 to $25\,\mathrm{cm\,s^{-1}}$, the ignition/extinction behaviour ceases, and steady flames are obtained. These flames assume an axisymmetric shape, concave towards the fresh mixture. As U_{IN} increases, they stabilize farther downstream until they are eventually blown out of the domain for $U_{IN} > 500\,\mathrm{cm\,s^{-1}}$. Three-dimensional iso-surfaces of Y_{OH} superimposed on the iso-contours and iso-lines of temperature in the y–z plane for flames at $U_{IN} = 175$, 350 and $450\,\mathrm{cm\,s^{-1}}$ in figure 6, clearly show the axisymmetric structure of the flame.

A closer look at the internal flame structure reveals that it changes as the inflow velocity is increased. For $U_{IN} < 75\,\mathrm{cm\,s^{-1}}$, the maxima of temperature and all species mass fractions are located on the tube axis ($r = 0$), as exemplified by the hydrogen radical mass fraction Y_{H} iso-contour (figure 7*a*). For $U_{IN} > 75\,\mathrm{cm\,s^{-1}}$, $Y_{\mathrm{H},max}$ shifts away from the axis onto a circle of radius increasing with U_{IN}: the four plots of figure 7 clarify this transition. The first appearance of a curved annular shaped flame, i.e. with the maximum value of Y_{O} and Y_{OH} located away from $r = 0$ is observed at significantly higher inflow velocities ($U_{IN} = 150$ and $175\,\mathrm{cm\,s^{-1}}$, respectively). The value of U_{IN} above which the maxima of the H, O and OH radical species move away from the tube axis, is marked by arrows in the flame stability diagram of figure 2,

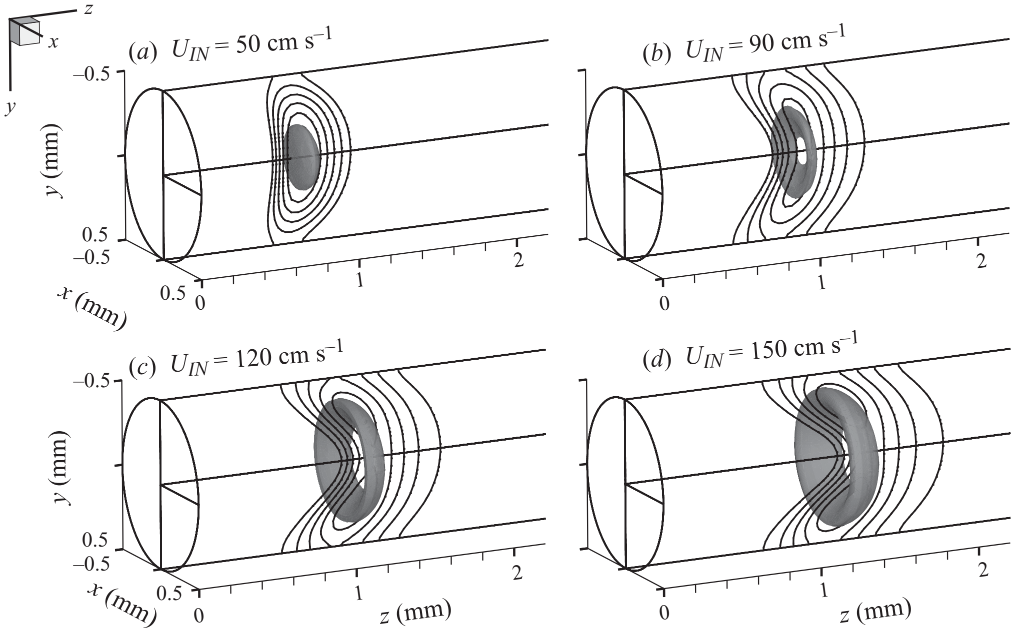

FIGURE 7. Steady axisymmetric flame in the $d = 1.0$ mm tube for inflow velocity (*a*) 50 cm s^{-1}, (*b*) 90 cm s^{-1}, (*c*) 120 cm s^{-1} and (*d*) 150 cm s^{-1}: iso-surfaces of Y_{H} ($Y_{\mathrm{H}} = 1.17 \times 10^{-4}$, 1.8×10^{-4}, 2.15×10^{-4} and 2.5×10^{-4}, in (*a–d*), respectively) superimposed on five iso-lines of Y_{H} on the $x = 0$ plane (ranging from 5.00×10^{-5} to 1.05×10^{-4}, 1.70×10^{-4}, 1.97×10^{-4}, 2.30×10^{-4} in (*a–d*), respectively).

showing that the radical species with the higher molecular diffusivity deviate first. The maxima of the temperature and the radicals HO_2 and H_2O_2 always remain on the tube axis. In experiments, the OH radical is typically considered as a marker of the flame front.

It is worth pointing out that a similar sequence of transition in the flame dynamics was observed in the planar simulations of Pizza *et al.* (2008*b*) for small enough channel heights.

4. Flame dynamics in the 1.5 mm diameter tube

In addition to the combustion modes found in the narrow tube, the richer flame dynamics in the $d = 1.5$ mm tube include the spinning and the non-axisymmetric flames described in detail below. For this wider tube, the steady axisymmetric flames are further distinguished as open and closed, when the maximum of the Y_{OH} is on or off-axis, respectively. The transitions observed upon variation of the inflow velocity are presented in figure 8. The parameter $\beta = (1 + s^n) r_{\mathrm{OH}max}/r$ on the y-axis has been constructed in order to qualitatively distinguish the various flame types, and can be explained with the help of the inset in figure 8. It combines information about the axial symmetry through s (the maximum separation in the streamwise flame anchoring positions measured using the $Y_{\mathrm{OH}} = 8 \times 10^{-4}$ iso-surface) and the open or closed structure of the flame through $r_{\mathrm{OH}max}$ (the radial distance from the axis of the location of maximum Y_{OH}). Both s and $r_{\mathrm{OH}max}$ are non-dimensionalized by the tube radius, and the exponent n is introduced to increase the sensitivity on s (here, $n = 0.1$). Thus, for the mild, ignition/extinction, as well as closed axisymmetric flames, $\beta = 0$

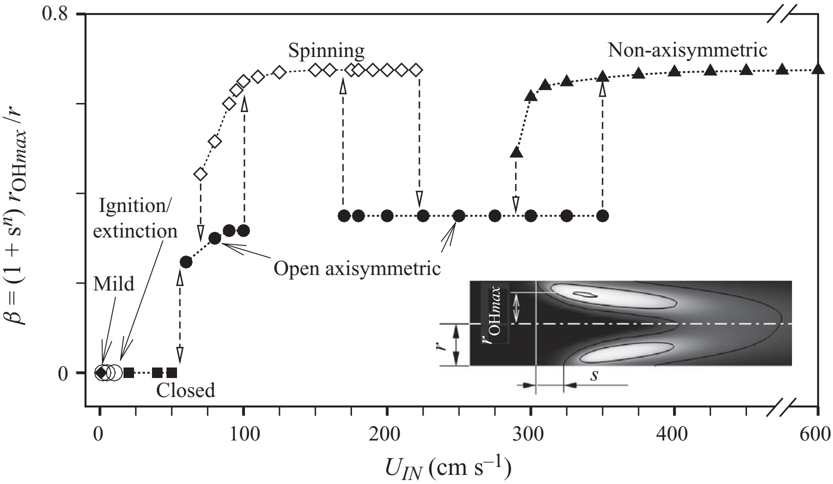

FIGURE 8. Flame stability diagram for the $d = 1.5$ mm tube. The distance s is the maximum displacement of the flame anchoring position with respect to the upstream edge of the $Y_{\mathrm{OH}} = 8 \times 10^{-4}$ iso-surface. The dashed lines with arrows indicate the observed transitions. The inset shows iso-contours of Y_{OH} around the flame, for the non-axisymmetric flame at $U_{IN} = 400\,\mathrm{cm\,s^{-1}}$, in the plane where s is computed. The parameter n is chosen as 0.1.

since $Y_{\mathrm{OH}max}$ is located on the tube axis. For these flames, s is also equal to zero, as they are all axisymmetric. The open axisymmetric flame (described in § 4.2), still with $s = 0$, can be distinguished from the closed one (see § 4.1) because $r_{\mathrm{OH}max} > 0$, and thus $\beta > 0$. For the steady non-axisymmetric (see § 4.4) and the spinning flames (see § 4.3) both s and $r_{\mathrm{OH}max}$ are greater than zero. In addition, since the spinning flame is characterized by a 'solid-body' rotation, the values of s and $r_{\mathrm{OH}max}$ remain constant in time.

The features of the mild combustion ($0.5 \leqslant U_{IN} \leqslant 1\,\mathrm{cm\,s^{-1}}$) and ignition/extinction mode ($2 \leqslant U_{IN} \leqslant 10\,\mathrm{cm\,s^{-1}}$) in the $d = 1.5$ mm tube are qualitatively similar to the $d = 1.0$ mm tube and will not be described again.

4.1. *Closed axisymmetric flames*

These flames are stable over the range $20 \leqslant U_{IN} \leqslant 50\,\mathrm{cm\,s^{-1}}$, and are steady and symmetric with respect to the tube axis. The name 'closed' denotes that the Y_{OH} distribution displays a single maximum on the tube axis (figure 9*a*). At $U_{IN} = 20\,\mathrm{cm\,s^{-1}}$ the maxima of temperature and of all species are located on the axis; at $U_{IN} = 40\,\mathrm{cm\,s^{-1}}$, $Y_{\mathrm{H},max}$ has already shifted away from the axis, followed by the $Y_{\mathrm{O},max}$ at $U_{IN} = 50\,\mathrm{cm\,s^{-1}}$. Finally, at $U_{IN} = 60\,\mathrm{cm\,s^{-1}}$ the Y_{OH} iso-surface assumes a ring shape, leading to the open axisymmetric flames described in the next section.

4.2. *Open axisymmetric flames*

The open axisymmetric flames are also steady. For $U_{IN} \approx 100\,\mathrm{cm\,s^{-1}}$ the location of the maximum of temperature shifts away from the axis, contrary to the $d = 1.0$ mm tube where the peak temperature was always located on the axis. Figure 9(*b*, *c*) illustrate examples of such flames at different U_{IN}. These flames appear over two disconnected ranges of inflow velocities: $60 \leqslant U_{IN} \leqslant 100\,\mathrm{cm\,s^{-1}}$ and $170 \leqslant U_{IN} \leqslant 350\,\mathrm{cm\,s^{-1}}$ (see figure 8). Starting with an open axisymmetric flame and varying the inflow velocity slightly above $100\,\mathrm{cm\,s^{-1}}$ or below $170\,\mathrm{cm\,s^{-1}}$, leads to flames exhibiting self-sustained oscillations, whereas upon increase of U_{IN} above the upper limit of the stability range

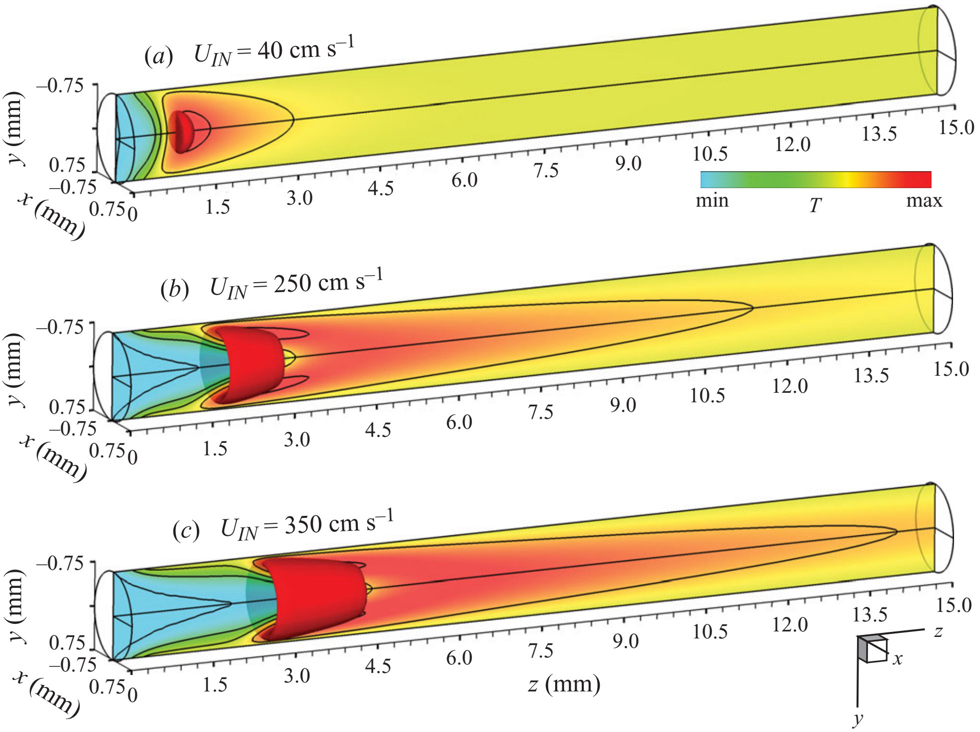

FIGURE 9. Closed (a) and open (b, c) axisymmetric flames in the $d = 1.5$ mm tube at three different inflow velocities ($U_{IN} = 40$, 250 and 350 cm s^{-1}): three-dimensional iso-surfaces of $Y_{OH} = 1.5 \times 10^{-3}$ in (a) and 2.3×10^{-3} in (b, c) and iso-contours of temperature on the $x = 0$ plane with five iso-lines uniformly distributed from 301 K to 1320 K, 1350 K and 1410 K, in (a–c) respectively.

(350 cm s^{-1}) the axisymmetric flames become unstable leading to non-axisymmetric flame structures.

4.3. *Spinning flames*

Starting with the steady open axisymmetric flame at $U_{IN} = 100$ cm s^{-1} and increasing the inflow velocity to 110 cm s^{-1} (or, similarly, after an impulsive decrease from $U_{IN} = 170$ to 160 cm s^{-1}), the flame assumes an asymmetric shape with respect to the tube axis, which rotates in the azimuthal direction while maintaining its structure.

Spinning flames exist in the range $70 \leqslant U_{IN} \leqslant 220$ cm s^{-1}. Some characteristics of this combustion mode for $U_{IN} = 150$ cm s^{-1} are shown in figure 10 after the initial transients have died out. The temporal evolution of the temperature at the reference point P with coordinates $x, y, z = 0.3$, 0.1, 2.06 mm, selected inside a region with appreciable temperature variation, and of the integral of the normalized heat release rate in the whole domain, HRR, can be seen in figure 10(a). Temperature at P varies between 894 and 1445 K, while HRR remains constant. The flame rotates like a solid body without changing its non-axisymmetric structure, as also illustrated by the $Y_{OH} = 1.7 \times 10^{-3}$ iso-surfaces at the four time instants t_1–t_4 (figure 10b,d,f,h). The corresponding distributions of Y_{OH} at the same time instants on the plane normal to $z = 1.5$ mm (figure 10c,e,g,i) indicate a clockwise flame rotation.

The flame rotation creates a complex swirling flow pattern (figure 11). On a plane normal to the axial direction (like the one shown at $z = 1.5$ mm), part of the mixture

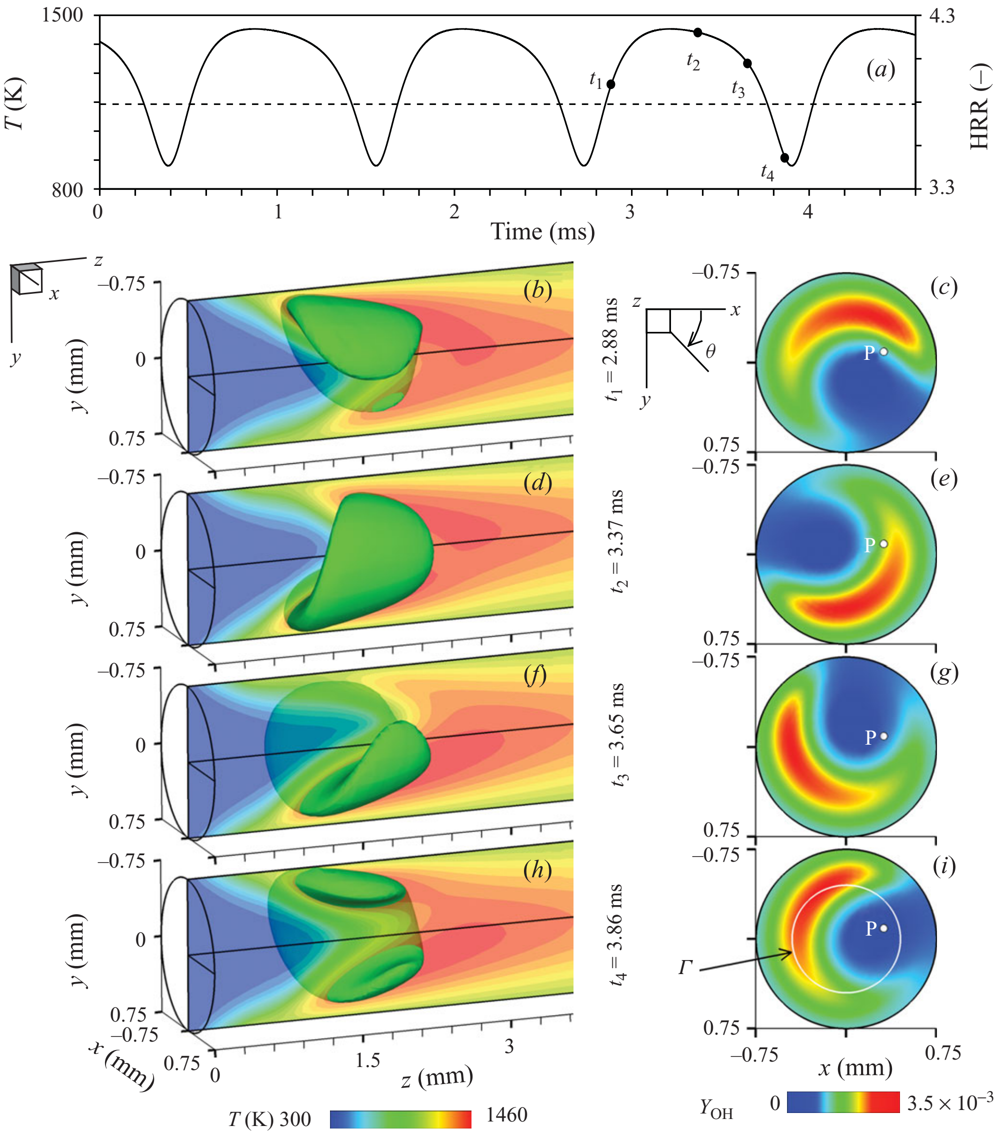

FIGURE 10. Clockwise spinning flame at $U_{IN} = 150\,\mathrm{cm\,s^{-1}}$ in the $d = 1.5$ mm tube: (a) temporal evolution of the temperature (solid line) at the reference point P with coordinates $(x, y, z) = (0.3,\ 0.1,\ 2.06)$ mm, and integral heat release HRR (dashed line); (b, d, f, h) iso-surfaces of $Y_{OH} = 1.7 \times 10^{-3}$, and temperature iso-contours on the y–z plane at the four times t_1 to t_4 marked in (a); (c, e, g, i) iso-contours of Y_{OH} on the $z = 1.5$ mm plane at time instances t_1–t_4.

flows in the counterclockwise direction, towards the flame, while another part flows in the clockwise direction. The magnitude of the velocity vector projected on this plane is less than $0.4U_{IN}$, much lower than the spinning azimuthal velocity of the flame itself, evaluated at a radius of 1.0 mm to be approximately $5U_{IN}$ (for the case of figure 11). This comparison implies that no significant rotation of the flow is caused by the spinning flame. Another interesting finding is that the radial and the azimuthal velocity components exhibit two points on this plane at which they are both equal to

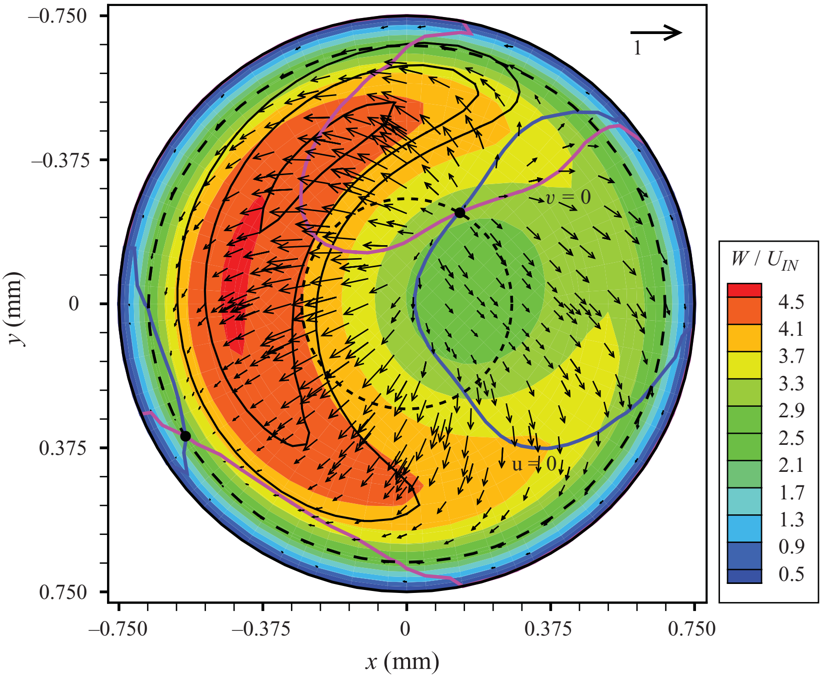

FIGURE 11. Cross-section at $z = 1.5$ mm extracted from the spinning flame at $U_{IN} = 150\,\mathrm{cm\,s^{-1}}$ at the time instant t_4 in figure 10(a): iso-contours of the non-dimensional axial velocity component w (the reference value is $U_{IN} = 150\,\mathrm{cm\,s^{-1}}$), velocity vectors on the z-plane, iso-lines of Y_{OH} at levels 2.00×10^{-3}, 2.75×10^{-3} and 3.50×10^{-3} (black solid lines), iso-lines of $u = 0$ and $v = 0$ (blue and magenta solid lines, respectively), velocity vectors. The two black dashed circles represent the loci of points where $u = v = 0$ during the azimuthal rotation of the flame.

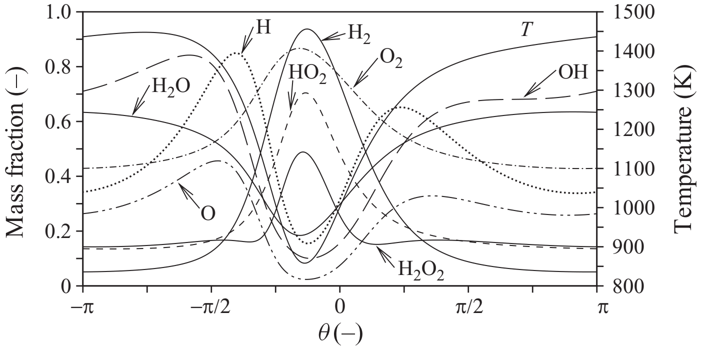

FIGURE 12. Spinning flame structure for $U_{IN} = 150\,\mathrm{cm\,s^{-1}}$ in the $d = 1.5$ mm tube at time instant t_4 (figure 10): species mass fractions ($17.2Y_{H_2}$, $4.4Y_{O_2}$, $4.6Y_{H_2O}$, $37.1Y_H$, $17.2Y_O$, $29.4Y_{OH}$, $41.6Y_{HO_2}$, $104.0Y_{H_2O_2}$) and temperature along the circle marked as Γ in figure 10(i) on the plane $z = 1.8$ mm. At this instant, the flame moves in the direction from positive to negative θ. The angle θ is defined to the right of figure 10(b).

zero; as the flame rotates, these two zero-velocity points move along the dashed circles shown in figure 11 (the circles mark the loci of the zero velocity points at all times).

The species and temperature profiles at the time instant t_4 extracted along the circle Γ of radius 0.45 mm on the $z = 1.8$ mm plane (indicated in figure 10i), are plotted in figure 12. The unburnt mixture ahead of the flame, $-\pi/4 < \theta < 0$ (the

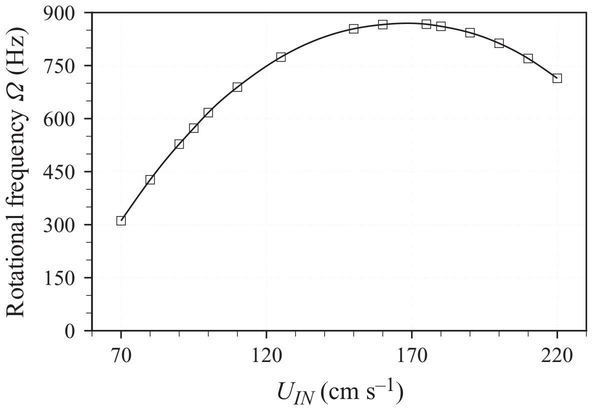

FIGURE 13. Spinning flames in the $d = 1.5$ mm tube: rotational frequency Ω (Hz) as a function of the inflow velocity U_{IN}.

angle $\theta = 0$ is arbitrarily taken to correspond to the positive x-axis and increases in the clockwise direction), is at a significantly higher temperature than the inflow temperature ($T \approx 900$ K compared to $T_{IN} = 300$ K), and the flame front propagates in a mixture rich in radicals. As a result, the azimuthal propagation velocity of the flame tip during rotation is found to be up to five times larger than the laminar flame speed S_L.

The variation of the rotational frequency of the spinning flame with the inflow velocity is presented in figure 13. As can be seen, this value is always larger than 300 Hz, justifying the use of fixed wall-temperature boundary conditions (the response time of the solid is typically much longer due to its large thermal inertia). The spinning mode coexists with the axisymmetric over a significant range of inflow velocities (figure 8) and the transition between the two modes is hysteretic.

4.4. *Steady non-axisymmetric flames*

As the inflow velocity is increased from $U_{IN} = 350$ to 375 cm s^{-1}, the open steady flame becomes unstable and a steady non-axisymmetric mode appears (figure 14), which is stable over the range $290 \leqslant U_{IN} \leqslant 600$ cm s^{-1} ($231 \leqslant Re_{IN} \leqslant 477$). As illustrated in figure 15 from the OH mass fraction and temperature azimuthal profiles along a circle of radius 0.45 mm on the $z = 6$ mm plane for the flame at $U_{IN} = 500$ cm s^{-1}, this combustion mode exhibits symmetry around a plane containing the tube axis. The plane of symmetry always includes the tube axis but it is not fixed: a small perturbation of the flame in figure 14 can lead to another steady non-axisymmetric flame solution rotated with respect to the original flame.

5. Axisymmetric simulations

In order to better understand the nature of some of the observed transitions, axisymmetric simulations were performed for the $d = 1.5$ mm tube using a two-dimensional axisymmetric mesh. These simulations allowed the computation of stable as well as otherwise unstable (in three-dimensional) axisymmetric solutions and facilitated the Fourier analysis of the transitions described in § 6. The combustion modes and the transitions observed by varying the inflow velocity are summarized in figure 16.

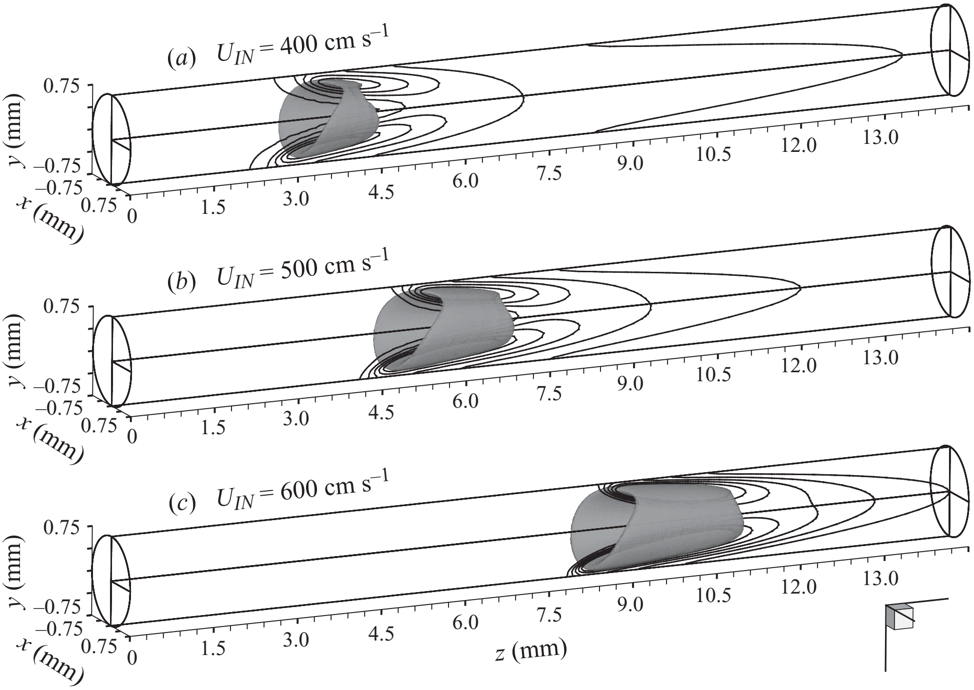

FIGURE 14. Steady non-axisymmetric flames in the $d = 1.5$ mm tube at three different inflow velocities ($U_{IN} = 400\,\mathrm{cm\,s^{-1}}$, $500\,\mathrm{cm\,s^{-1}}$ and $600\,\mathrm{cm\,s^{-1}}$): iso-surfaces of $Y_{\mathrm{OH}} = 3.38 \times 10^{-3}$, superimposed on five equi-spaced Y_{OH} iso-lines on the $x = 0$ plane in the ranges $1.0 \times 10^{-4} \leqslant Y_{\mathrm{OH}} \leqslant 3.0 \times 10^{-3}$, $5.0 \times 10^{-4} \leqslant Y_{\mathrm{OH}} \leqslant 3.0 \times 10^{-3}$ and $1.1 \times 10^{-3} \leqslant Y_{\mathrm{OH}} \leqslant 3.0 \times 10^{-3}$ in (a, b, c), respectively.

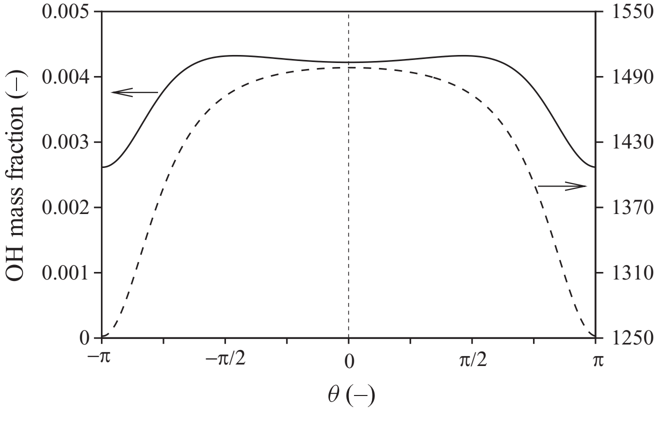

FIGURE 15. Steady non-axisymmetric flame at $U_{IN} = 500\,\mathrm{cm\,s^{-1}}$: OH mass fraction (solid line) and temperature (dashed line) profiles extracted from the plane at $z = 6$ mm at a radius of 0.45 mm. The axis orientation has been adjusted in order to shift the plane of symmetry of this flame to $\theta = 0$.

The mild combustion ($0.5 \leqslant U_{IN} \leqslant 1.0\,\mathrm{cm\,s^{-1}}$), ignition/extinction ($2 \leqslant U_{IN} \leqslant 17\,\mathrm{cm\,s^{-1}}$) and the steady open and closed axisymmetric modes ($13 \leqslant U_{IN} \leqslant 57\,\mathrm{cm\,s^{-1}}$ and $128 \leqslant U_{IN} \leqslant 600\,\mathrm{cm\,s^{-1}}$) are also obtained in the axisymmetric simulations, and their structure is identical to the three-dimensional case described in the previous section.

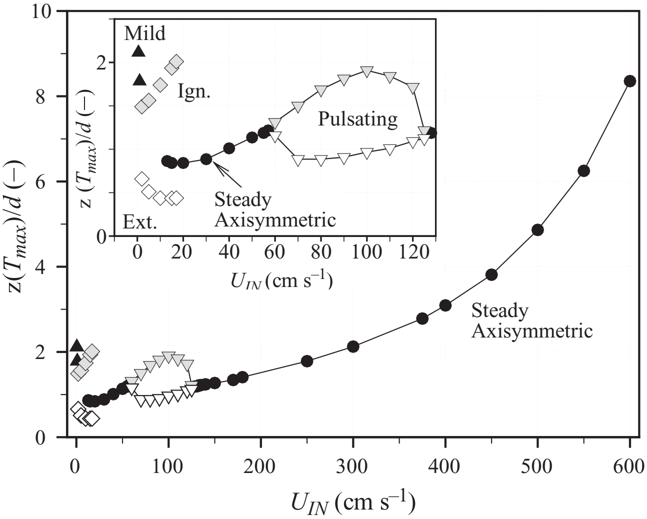

FIGURE 16. Flame stability diagram of the flames in the $d = 1.5$ mm axisymmetric domain in terms of the normalized streamwise distance of the maximum temperature location versus the inflow velocity. The combustion modes at low U_{IN} are more clearly shown in the enlarged inset: diamonds mark the $z(T_{max})/d$ at ignition and extinction, whereas triangles mark the extreme streamwise locations of the pulsating mode.

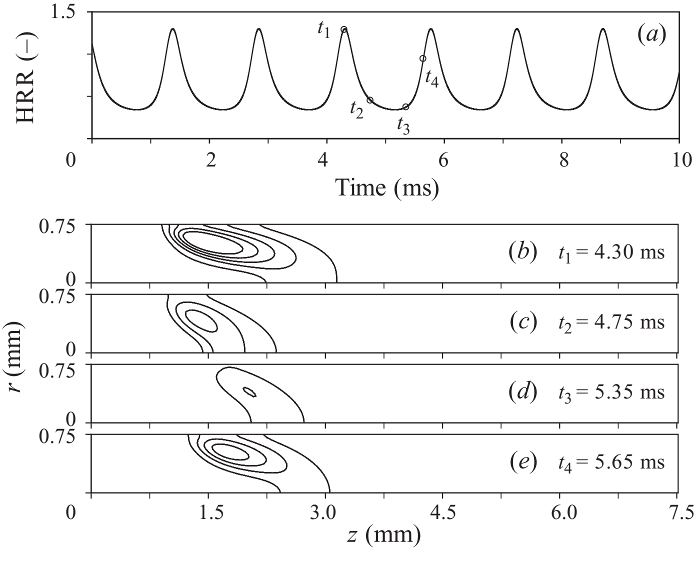

FIGURE 17. Pulsating flame at $U_{IN} = 100\,\mathrm{cm\,s^{-1}}$ in the $d = 1.5$ mm axisymmetric simulations: (a) temporal variation of the integral heat release rate HRR; (b–e) five iso-lines of Y_{OH} (ranging from $Y_{OH} = 6.3 \times 10^{-4}$ to $Y_{OH} = 2.5 \times 10^{-3}$ at equal increments) at the four times t_1–t_4 marked in (a). The missing iso-lines in (c–e) indicate higher values of Y_{OH} at t_1.

At an intermediate range of inflow velocities, a new oscillatory mode not observed in the three-dimensional domain is obtained. For $59 \leqslant U_{IN} \leqslant 125\,\mathrm{cm\,s^{-1}}$, the axisymmetric flames pulsate in the streamwise direction. Details of the pulsating flame structure at $U_{IN} = 100\,\mathrm{cm\,s^{-1}}$ are given in figure 17. Figure 17(b–e) provides iso-lines of Y_{OH} at the four time instances marked in the temporal evolution profile

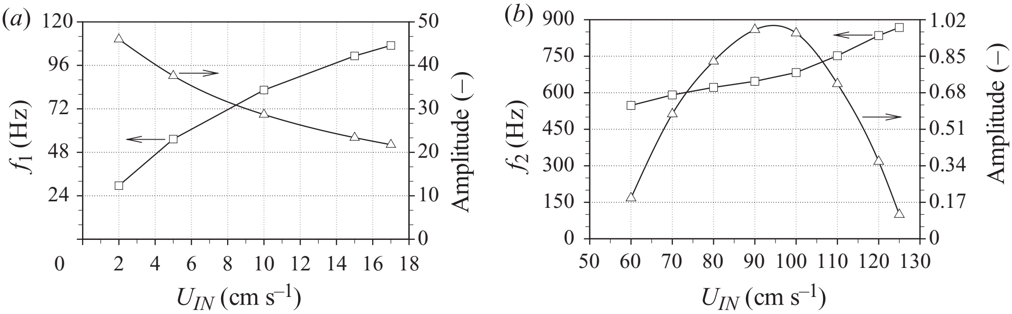

FIGURE 18. Frequency (squares) and amplitude of HRR (triangles) of (*a*) the ignition/extinction (f_1) and (*b*) the pulsating mode (f_2) as a function of the inflow velocity.

of HRR (figure 17*a*). The flame moves back and forth in the streamwise direction, with the combustion intensity increasing as the flame propagates upstream, towards richer mixtures (figure 17*b*,*e*), and weakening as it travels downstream (figure 17*c*,*d*).

The considerably lower computational cost of the axisymmetric simulations, allows for more precise determination of the critical inflow velocity values for the transitions between the different modes. As clearly seen in figure 16, the transitions from steady axisymmetric to the pulsating flames on the two extremes of the stability range of pulsating flames, are supercritical. The ignition/extinction and the steady axisymmetric flames coexist over a narrow range of U_{IN}, and the transition is subcritical.

The HRR frequencies and amplitudes of the ignition/extinction and pulsating modes as a function of U_{IN} are plotted in figures 18(*a*) and 18(*b*), respectively. The quadratic increase from zero (steady to pulsating flames at the extrapolated value $U_{IN} \approx 57\,\text{cm}\,\text{s}^{-1}$, figure 18*b*), and decrease to zero (pulsating to steady at the extrapolated value $U_{IN} \approx 128\,\text{cm}\,\text{s}^{-1}$, figure 18*b*) of the pulsation amplitude with the distance from the critical points indicate that these transitions result from supercritical Hopf bifurcations, while the ignition/extinction to steady flame transition (at $U_{IN} \approx 17\,\text{cm}\,\text{s}^{-1}$, figure 18*a*) results from a subcritical Hopf bifurcation. It is worth pointing out that there is almost an order of magnitude difference in the frequencies of the two modes, which is most likely related to the order of magnitude difference of the corresponding U_{IN} ranges. Finally, for the same U_{IN}, the frequency of the ignition/extinction mode is slower in the wider tube (compare the 158 Hz of the 1.0 mm tube in § 3.2 with the 82 Hz of the 1.5 mm tube in figure 18(*a*) at $10\,\text{cm}\,\text{s}^{-1}$). This is due to the faster preheat of the inflowing reacting mixture in the narrow tube.

6. Fourier analysis of the transitions

In order to gain deeper insight into the transitions from the axisymmetric to the spinning and to the steady non-axisymmetric flames, Fourier analysis was employed. Using spectral polynomial interpolation, the corresponding solution obtained with the two-dimensional axisymmetric code was interpolated onto the three-dimensional mesh and was used as an initial condition for a new three-dimensional simulation. The numerical noise introduced by the interpolation was sufficient to trigger the transitions, and, depending on the value of U_{IN}, the solution evolved to different combustion modes. During the transition, the variables were expanded in Fourier

Case	U_{IN} (cm s^{-1})	Axi	Three-dimensional starting from Axi IC
1	250	Steady axisymmetric	Steady axisymmetric
2	150	Steady axisymmetric	Spinning
3	400	Steady axisymmetric	Steady non-axisymmetric with planar symmetry

Table 1. Solutions obtained at different U_{IN} with axisymmetric simulations (Axi), and with full three-dimensional simulations using the axisymmetric solution as initial condition (three-dimensional with Axi IC).

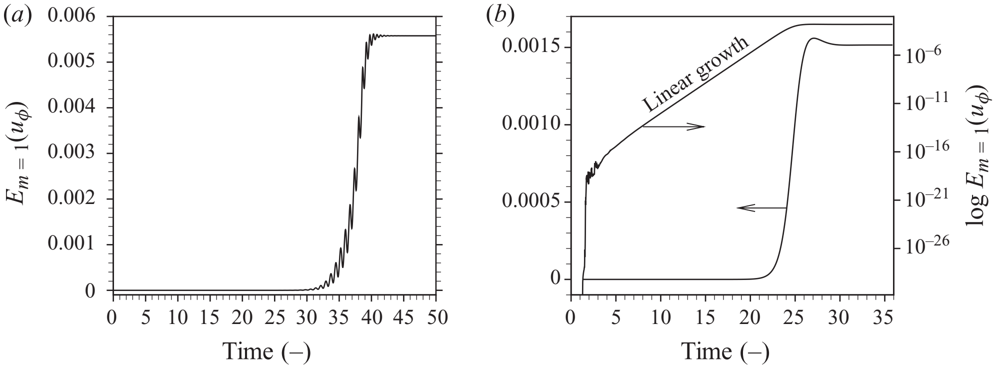

Figure 19. Non-dimensional time history of the energy of the $m=1$ mode of u_ϕ for (*a*) case 2 and (*b*) case 3 (table 1).

series in the azimuthal direction:

$$g(z, r, \phi, t) = \sum_{m=0}^{M-1} g_m(r, z, t)\mathrm{e}^{\mathrm{i}m\phi}, \tag{6.1}$$

where m represents the azimuthal Fourier mode and g denotes any physical variable. The total energy of all non-axisymmetric modes for all variables was followed in time, together with the magnitude of their real and imaginary parts and azimuthal energy spectra.

Table 1 summarizes the conditions analysed. When the steady axisymmetric flame at $U_{IN} = 250\,\mathrm{cm\,s^{-1}}$ is used as initial condition, the solution obtained with the three-dimensional code is still steady and axisymmetric (case 1). Thus, the $m=0$ mode is the only mode present at this value of U_{IN} and is the only one obtained with axisymmetric (figure 16) and with three-dimensional simulations (figure 8). In this case, the energy of the $m=0$ mode remains practically constant in time indicating the stability of the initial axisymmetric solution, whereas the $m=1$ mode has practically zero energy.

On the other hand, the steady axisymmetric flames at $U_{IN} = 150$ (case 2) and $400\,\mathrm{cm\,s^{-1}}$ (case 3), obtained using the axisymmetric code, are not three-dimensional stable. When used as initial conditions for three-dimensional simulations, the outcome is a spinning (case 2), or a steady non-axisymmetric flame with planar symmetry (case 3).

Figure 19(*a*) shows the non-dimensional time history of the $m=1$ mode energy for the transition from axisymmetric to spinning flame (case 2, table 1). The oscillations

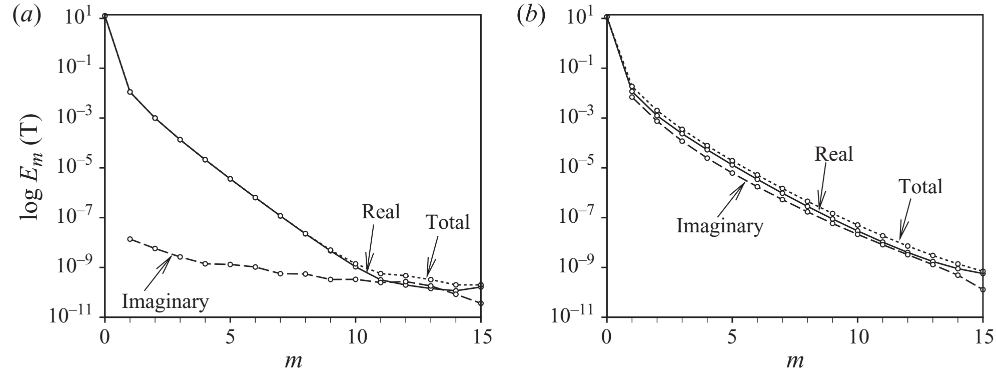

FIGURE 20. Instantaneous azimuthal energy spectrum of temperature as function of wavenumber m, for (a) the non-axisymmetric flame with planar symmetry at $U_{IN} = 500\,\mathrm{cm\,s^{-1}}$ and (b) the spinning flame at $U_{IN} = 150\,\mathrm{cm\,s^{-1}}$, showing total energy (dashed line) as well as the real (solid line) and imaginary parts (long-dashed line) of the energy.

superimposed on the exponential growth regime indicate that another oscillating mode is active during this transition, which however decays in time. Indeed, closer examination of the isosurfaces of temperature during the exponential growth reveals that the flame base exhibits small-amplitude high-frequency decaying oscillations.

For case 3, figure 19(b) shows the non-dimensional time history of the $m = 1$ mode energy. After a stage of exponential growth (associated with the linear mode) and nonlinear saturation, the solution evolves to the three-dimensional steady non-axisymmetric flame with planar symmetry discussed in § 4.4. Further evidence of the planar symmetry of this steady non-axisymmetric flame is given in figure 20(a) where the azimuthal mode energy for temperature is plotted as a function of the wave number m, together with the magnitude of its real and imaginary parts, after adjusting the phase θ so that $\theta = 0$ coincides with the plane of symmetry. As can be observed, only the real part of the dominant azimuthal modes has a significant energy level for the steady non-axisymmetric flame with planar symmetry, whereas the imaginary part is at least three orders of magnitude smaller. In the case of the spinning flame, no phase angle could be found making the real or the imaginary part of the energy significantly smaller than the other (figure 20b). Since both real and imaginary parts of the energy spectrum are of the same order of magnitude for all phase angles, the spinning flame contains no planar symmetry.

7. Conclusions

The dynamics of lean hydrogen/air premixed flames in cylindrical tubes with diameters $d = 1.0$ and 1.5 mm were investigated using numerical simulation with detailed chemistry and transport. The focus was on the identification of the stable combustion modes and the transitions between different flame structures as the inflow velocity is varied so as to cover all possible flame positions inside a domain of length $L = 10d$.

In the smaller diameter tube, only axisymmetric flames are obtained. As U_{IN} increases, the flames undergo transitions from mild combustion, to periodic ignition/extinction and finally to steady axisymmetric flames. The internal structure of the latter mode can be different: at low inflow velocities, the maxima of all species mass fractions and temperatures are located on the axis of symmetry. At higher velocities, the maxima of the lighter, more mobile species (H, O, OH) move away from the axis. Similar dynamics were observed in the planar simulations of Pizza *et al.* (2008*b*) in microchannels with a height greater than 0.6 mm, as well as in other experimental (Maruta *et al.* 2005; Richecoeur & Kyritsis 2005) and numerical studies with simplified models (Maruta *et al.* 2005; Jackson *et al.* 2007; Kurdyumov *et al.* 2009).

In the wider tube, more complex dynamics are observed. In addition to the flame structures found in the narrow channel, non-axisymmetric modes are obtained: a steady non-axisymmetric flame which is characterized by planar symmetry, and a spinning flame which rotates azimuthally with high frequency as a 'solid body' three-dimensional structure. This mode, which has not been previously obtained computationally, is similar to that observed in the methane/air and propane/air diverging tube experiments of Xu & Ju (2007). The spinning frequencies ranged between 311 and 867 Hz, and were an order of magnitude faster than the frequencies of the ignition extinction mode. Over extended ranges of U_{IN}, the spinning mode was observed to coexist with the axisymmetric mode; the bifurcations between the two modes are therefore subcritical. Another case of multi-stability and subcritical bifurcations was found between axisymmetric and non-axisymmetric flames. The results confirm the existence of a critical tube diameter (between 1.0 and 1.5 mm), below which only axisymmetric flame shapes are possible, in agreement with numerical work in two-dimensional microscale channels (Pizza *et al.* 2008*b*) and three-dimensional tubes (Kurdyumov & Fernandez-Tarrazo 2002), and with theoretical results (Matkowsky & Olagunju 1982; Petchenko & Bychkov 2004).

Axisymmetric simulations were performed to compute flames that are three-dimensional stable or unstable and to study the transitions from axisymmetric to three-dimensional structures. The significantly cheaper axisymmetric simulations verified the range of stability of the three-dimensional steady axisymmetric flames shown in figure 8, and revealed the existence of a new (three-dimensional unstable) combustion mode exhibiting streamwise pulsations, which appear and disappear at supercritical Hopf bifurcations. The stability of the axisymmetric solutions in the full domain was investigated by using them as initial conditions for three-dimensional simulations. Fourier analysis in the azimuthal direction performed during the flame evolution demonstrated the dominance of the $m = 1$ azimuthal mode in both the steady non-axisymmetric flame with planar symmetry as well as in the spinning flame with 'solid-body'-like rotation. Comparison of real and imaginary parts in the energy of each mode, properly adjusting the phase angle, verified the existence of planar symmetry in the stationary three-dimensional non-axisymmetric flame; this type of symmetry was absent in the spinning flame.

Mapping the detailed flame dynamics in microtubes or microchannels is of fundamental as well as applied interest, since they can be potentially harmful in microdevices: for example, oscillatory combustion modes can compromise the reactor integrity, while steady non-axisymmetric flames require longer lengths to complete combustion compared to symmetric conical flames anchored at the same upstream position. The observed dynamics is expected to be sensitive to the wall temperature (considered to be fixed in this study), as well as the fresh mixture composition. The range of operating conditions over which the dynamics reported here persist will be the focus of a future paper. Recent code developments to address the conjugate heat transfer in the solid walls will also allow consideration of additional physical processes that can affect the system dynamics.

Financial support has been provided by the Swiss National Foundation project number 200021-109398. G.P. is grateful to Stefan Kerkemeier for his help with coding. A.G.T. would like to acknowledge support from the Greek Secreteriat of Research and Technology.

REFERENCES

Bychkov, V., Akkerman, V., Fru, G., Petchenko, A. & Eriksson, L.-E. 2007 Flame acceleration in the early stages of burning in tubes. *Combust. Flame* **150**, 263–276.

Chu, B.-T. & Kovasznay, C. 1958 Non-linear interactions in a viscous heat-conducting compressible gas. *J. Fluid Mech.* **3**, 494–514.

Clanet, C. & Searby, G. 1996 On the 'tulip flame' phenomenon. *Combust. Flame* **105**, 225–238.

Coffee, T. P. & Heimerl, J. M. 1981 Transport algorithms for premixed laminar steady-state flames. *Combust. Flame* **43**, 273–289.

Cohen, S. D. & Hindmarsh, A. C. 1996 CVODE, a stiff/nonstiff ODE solver. *Comput. Phys.* **10** (2), 138–143.

Deville, M. O., Fischer, P. F. & Mund, E. H. 2002 *High-Order Methods for Incompressible Fluid Flows*. Cambridge University Press.

Dogwiler, U., Mantzaras, J., Benz, P., Kaeppeli, B., Bombach, R. & Arnold, A. 1998 Homogeneous ignition of methane–air mixtures over platinum: comparison of measurements and detailed numerical predictions. *Proc. Combust. Inst.* **27**, 2275–2282.

Dunn-Rankin, D. & Sawyer, R. F. 1998 Tulip flames: changes in shape of premixed flames propagating in closed tubes. *Exp. Fluids* **24**, 130–140.

Dunn-Rankin, D., Sawyer, R. F. & Barr, P. K. 1986 Numerical and experimental study of 'tulip' flame formation in a closed vessel. *Proc. Combust. Inst.* **21**, 1291–1301.

Ellis, O. C. de C. 1928 Flame movement in gaseous explosive mixtures. *J. Fuel Sci.* **7**, 502–508.

Fischer, P. F., Lottes, J. W. & Kerkemeier, S. G. 2008 nek5000 Web page, http://nek5000.mcs.anl.gov.

Gonzalez, M., Borghi, B. & Saouab, A. 1992 Interaction of a flame front with its self-generated flow in an enclosure: the 'tulip flame' phenomenon. *Combust. Flame* **88**, 201–220.

Hirschfelder, J. O., Curtiss, C. F. & Bird, R. B. 1954 *Molecular Theory of Gases and Liquids*. Wiley.

Jackson, T. L., Buckmaster, J., Lu, Z., Kyritsis, D. C. & Massa, L. 2007 Flames in narrow circular tubes. *Proc. Combust. Inst.* **31**, 955–962.

Karagiannidis, S., Mantzaras, J., Jackson, G. & Boulouchos, K. 2007 Hetero-/homogeneous combustion and stability maps in methane-fueled catalytic microreactors. *Proc. Combust. Inst.* **31**, 3309–3317.

Kee, R. J., Dixon-Lewis, G., Warnatz, J., Coltrin, M. E. & Miller, J. A. 1986 A Fortran computer code package for the evaluation of gas-phase multicomponent transport properties. *Tech. Rep.* SAND86-8246. Sandia National Laboratories.

Kee, R. J., Grcar, J. F., Smoke, M. D. & Miller, J. A. 1985 PREMIX: a Fortran program for modeling steady laminar one-dimensional premixed flames. *Tech. Rep.* SAND85-8240. Sandia National Laboratories.

Kee, R. J., Rupley, F. M. & Miller, J. A. 1989 Chemkin. Part II. A Fortran chemical kinetics package for the analysis of gas-phase chemical kinetics. *Tech. Rep.* SAND89-8009B. Sandia National Laboratories.

Kim, T. J., Yetter, R. A. & Dryer, F. L. 1994 New results on moist CO oxidation: high pressure, high temperature experiments and comprehensive kinetic modeling. *Proc. Combust. Inst.* **25**, 759–766.

Kurdyumov, V. & Fernandez-Tarrazo, E. 2002 Lewis number effect on the propagation of premixed laminar flames in narrow open ducts. *Combust. Flame* **128**, 382–394.

Kurdyumov, V., Fernandez-Tarrazo, E., Truffaut, J.-M., Quinard, J., Wangher, A. & Searby, G. 2007 Experimental and numerical study of premixed flame flashback. *Proc. Combust. Inst.* **31**, 1275–1282.

Kurdyumov, V., Pizza, G., Frouzakis, C. E. & Mantzaras, J. 2009 Dynamics of premixed flames in a narrow channel with a step-wise wall temperature. *Combust. Flame* **156** (11), 2190–2200.

Kurdyumov, V., Truffaut, J.-M., Quinard, J., Wangher, A. & Searby, G. 2008 Oscillations of premixed flames in tubes near the flashback condition. *Combust. Sci. Technol.* **180**, 731–742.

Kwon, M. J., Lee, B. J. & Chung, S. H. 1996 An observation of near-planar spinning premixed flames in a sudden expansion tube. *Combust. Flame* **105**, 180–188.

Lewis, B. & von Elbe, G. 1987 *Combustion, Flames and Explosions in Gases*. Academic Press.

Majda, A. 1984 *Compressible Fluid Flow and Systems of Conservation Laws in Several Space Variables*. Springer.

Maksimov, Y. M., Pak, A. T., Lavrenchuk, G. B., Naiborodenko, Y. S. & Merzhanov, A. G. 1979 Spin combustion of gasless systems. *Combust. Expl. Shock Waves* **15**, 415–418.

Mantzaras, J. & Appel, C. 2002 Effects of finite rate heterogeneous kinetics on homogeneous ignition in catalytically stabilized channel flow combustion. *Combust. Flame* **130**, 336–351.

Marra, F. S. & Continillo, G. 1996 Numerical study of premixed laminar flame propagation in a close tube with a full Navier–Stokes approach. *Proc. Combust. Inst.* **26**, 907–913.

Maruta, K., Kataoka, T., Kim, N. I., Minaev, S. & Fursenko, R. 2005 Characteristics of microscale combustion in a narrow channel with a temperature gradient. *Proc. Combust. Inst.* **30**, 2429–2436.

Maruta, K., Takeda, K., Ahn, J., Borer, K., Sitzki, L., Ronney, P. D. & Deutschmann, O. 2002 Extinction limits of catalytic combustion in microchannels. *Proc. Combust. Inst.* **29**, 957–963.

Matalon, M. & Metzener, P. 1997 The propagation of premixed flames in closed tubes. *J. Fluid Mech.* **336**, 331–350.

Matkowsky, B. J. & Olagunju, D. O. 1982 Spinning waves in gaseous combustion. *SIAM J. Appl. Math.* **42**, 1138–1156.

Metzener, P. & Matalon, M. 2001 Premixed flames in closed cylindrical tubes. *Combust. Theory Model.* **5**, 463–483.

Minaev, S., Maruta, K. & Fursenko, R. 2007 Nonlinear dynamics of flame in a narrow channel with a temperature gradient. *Combust. Theory Model* **11** (2), 187–203.

Norton, D. G. & Vlachos, D. G. 2003 Combustion characteristics and flame stability at the microscale: a cfd study of premixed methane/air mixtures. *Chem. Engng Sci.* **58** (21), 4871–4882.

Panfilov, V., Bayliss, A. & Matkowsky, B. J. 2003 Spiral flames. *Appl. Math. Lett.* **16**, 131–135.

Patera, A. T. 1984 A spectral element method for fluid dynamics: laminar flow in a channel expansion. *J. Comput. Phys.* **54**, 468–488.

Pearlman, H. 1997 Excitability in high-Lewis number premixed gas combustion. *Combust. Flame* **109**, 382–398.

Petchenko, A. & Bychkov, V. 2004 Axisymmetric versus non-axisymmetric flames in cylindrical tubes. *Combust. Flame* **136**, 429–439.

Pizza, G., Frouzakis, C. E., Mantzaras, J., Tomboulides, A. G. & Boulouchos, K. 2008*a* Dynamics of premixed hydrogen/air flames in mesoscale channels. *Combust. Flame* **155**, 2–20.

Pizza, G., Frouzakis, C. E., Mantzaras, J., Tomboulides, A. G. & Boulouchos, K. 2008*b* Dynamics of premixed hydrogen/air flames in microchannels. *Combust. Flame* **152**, 433–450.

Pizza, G., Mantzaras, J., Frouzakis, C. E., Tomboulides, A. G. & Boulouchos, K. 2009 Suppression of combustion instabilities of premixed hydrogen/air flames in microchannels using heterogeneous reactions. *Proc. Combust. Inst.* **32**, 3051–3058.

Raja, L. L., Kee, R. J., Deutschmann, O., Warnatz, J. & Schmidt, L. D. 2000 A critical evaluation of Navier–Stokes, boundary-layer, and plug-flow models of the flow and chemistry in a catalytic-combustion monolith. *Catal. Today* **59**, 47–60.

Rehm, R. G. & Baum, H. R. 1978 The equations of motion for thermally driven buoyant flows. *J. Res. Natl Bur. Stand.* **83**, 297–308.

Richecoeur, F. & Kyritsis, D. C. 2005 Experimental study of flame stabilization in low Reynolds and Dean number flows in curved mesoscale ducts. *Proc. Combust. Inst.* **30**, 2419–2427.

Robbins, K., Gorman, M., Bowers, J. & Brockman, R. 2004 Spiral dynamics of pulsating methane-oxygen flames on a circular burner. *Chaos* **14**, 467–476.

Scott, S. K., Wang, J. & Showalter, K. 1997 Modelling studies of spiral waves and target pattern in premixed flames. *J. Chem. Soc. Faraday Trans.* **93**, 1733–1739.

Tomboulides, A. G., Lee, J. & Orszag, S. A. 1997 Numerical simulation of low Mach number reactive flows. *J. Sci. Comput.* **12**, 139–167.

Tomboulides, A. G. & Orszag, S. A. 1998 A quasi-two-dimensional benchmark problem for low Mach number compressible codes. *J. Comput. Phys.* **146** (2), 691–706.

Tsai, C.-H. 2008 The asymmetric behavior of steady laminar flame propagation in ducts. *Combust. Sci. Technol.* **180**, 533–545.

Xu, B. & Ju, Y. 2007 Experimental study of spinning combustion in a mesoscale divergent channel. *Proc. Combust. Inst.* **31**, 3285–3292.

Zamashchikov, V. V. 2003 Rotating gas flames. *Combust. Exp. Shock Waves* **39**, 124–125.

Zhang, S. & Munir, Z. A. 1992 Spin combustion in the nickel-silicon system. *J. Mater. Sci.* **27**, 5789–5794.